



Landsat, MODIS, and VIIRS snow cover mapping algorithm performance as validated by airborne lidar datasets

Timbo Stillinger¹, Karl Rittger^{1,2}, Mark S. Raleigh³, Alex Michell¹, Robert E. Davis⁴, and Edward H. Bair¹

¹Earth Research Institute, University of California at Santa Barbara, Santa Barbara, CA 93106, USA

²Institute of Arctic and Alpine Research, University of Colorado Boulder, Boulder, CO 80309, USA

³College of Earth, Ocean, and Atmospheric Sciences, Oregon State University, Corvallis, OR 97331, USA

⁴Cold Regions Research and Engineering Laboratory, Hanover, NH 03755, USA

Correspondence: Timbo Stillinger (tcs@ucsb.edu)

Received: 3 August 2022 – Discussion started: 15 August 2022

Revised: 23 December 2022 – Accepted: 27 December 2022 – Published: 8 February 2023

Abstract. Snow cover mapping algorithms utilizing multi-spectral satellite data at various spatial resolutions are available, each treating subpixel variation differently. Past evaluations of snow mapping accuracy typically relied on satellite data collected at a higher spatial resolution than the data in question. However, these optical data cannot characterize snow cover mapping performance under forest canopies or at the meter scale. Here, we use 3 m spatial resolution snow depth maps collected on 116 d by an aerial laser scanner to validate band ratio and spectral-mixture snow cover mapping algorithms. Such a comprehensive evaluation of sub-canopy snow mapping performance has not been undertaken previously. The following standard (produced operationally by an agency) products are evaluated: NASA gap-filled Moderate Resolution Imaging Spectroradiometer (MODIS) MOD10A1F, NASA gap-filled Visible Infrared Imaging Radiometer Suite (VIIRS) VNP10A1F, and United States Geological Survey (USGS) Landsat 8 Level-3 Fractional Snow Covered Area. Two spectral-unmixing approaches are also evaluated: Snow-Covered Area and Grain Size (SCAG) and Snow Property Inversion from Remote Sensing (SPIReS), both of which are gap-filled MODIS products and are also run on Landsat 8. We assess subpixel snow mapping performance while considering the fractional snow-covered area (fSCA), canopy cover, sensor zenith angle, and other variables within six global seasonal snow classes. Metrics are calculated at the pixel and basin scales, including the root-mean-square error (RMSE), bias, and F statistic (a detection measure). The newer MOD10A1F Version 61 and VNP10A1F Version 1 product biases (-7.1% , -9.5%)

improve significantly when linear equations developed for older products are applied (2.8% , -2.7%) to convert band ratios to fSCA. The F statistics are unchanged (94.4% , 93.1%) and the VNP10A1F RMSE improves (18.6% to 15.7%), while the MOD10A1F RMSE worsens (12.7% to 13.7%). Consistent with previous studies, spectral-unmixing approaches (SCAG, SPIReS) show lower biases (-0.1% , -0.1%) and RMSE (12.1% , 12.0%), with higher F statistics (95.6% , 96.1%) relative to the band ratio approaches for MODIS. Landsat 8 products are all spectral-mixture methods with low biases (-0.4% to 0.3%), low RMSE (11.4% to 15.8%), and high F statistics (97.3% to 99.1%). Spectral-unmixing methods can improve snow cover mapping at the global scale.

1 Introduction

Snow cover is a globally significant climate forcing (Hansen and Nazarenko, 2004) and provides the water supply for billions of people (Mankin et al., 2015). Dramatic shifts in water availability are projected over the next 50 years due to climate change (Mankin et al., 2015; Immerzeel et al., 2020, 2010) and resulting from regional disturbances that accelerate snowmelt timing (e.g., dust on snow; Deems et al., 2013a; Skiles et al., 2012). As regions warm, the fraction of precipitation that falls as rain, rather than as snow, increases (Serquet et al., 2011; Feng and Hu, 2007), and glacial ice melts increasingly rapidly and disappears (Stewart et al., 2005; Zemp et al., 2015). Understanding the recent trends in

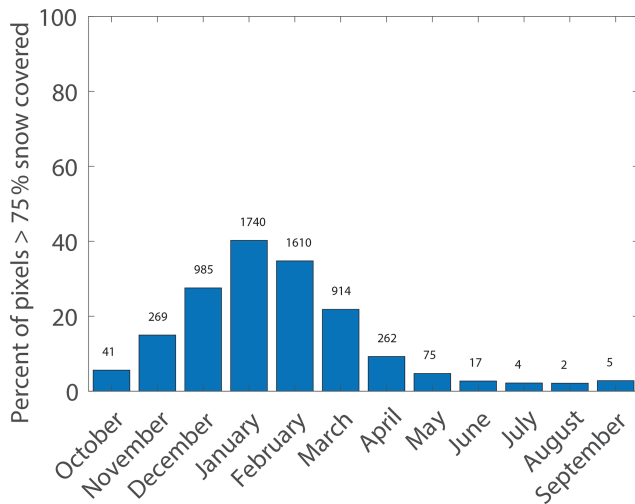


Figure 1. Percent of all snow-covered pixels with > 75 % viewable fSCA in the western USA averaged from 2001 to 2021 from the spatially and temporally complete MODIS Snow-Covered Area and Grain Size (STC-MODSCAG) product (Rittger et al., 2020). The number above each bar represents the snow cover extent in square kilometers averaged over the month of measurement. Pixels correspond to a 463 m spatial resolution.

Bormann et al. (2018) and trajectory of global snow cover is critical for comprehending global climate change and its impacts.

At the regional to global scales, satellite remote sensing is the best tool for measuring snow cover and snow albedo across landscapes (Molotch et al., 2004; Lettenmaier et al., 2015; Bair et al., 2019). The capability to map snow cover from space was realized early in the era of spaceborne remote sensing (Dozier et al., 1981; Warren, 1982), and spaceborne multispectral instruments are now routinely used to monitor many snow surface properties: the fractional snow-covered area (fSCA), snow albedo, snow grain size, reduction in albedo from light-absorbing particles (LAPs), and snow surface temperature (Painter et al., 2009, 2012; Lundquist et al., 2018; Bair et al., 2019; Nolin, 2010). Furthermore, remotely sensed snow cover information can be used to derive a variety of snow metrics that are relevant to the changing climate and to hydrologic systems (Nolin et al., 2021). These metrics and snow surface properties have been used to estimate persistent ice cover (Painter et al., 2012), analyze the impacts of wildfire on snowmelt (Micheletty et al., 2014), evaluate continental climate models (Minder et al., 2016), force regional climate models (Oaida et al., 2019), partition snowmelt and glacier melt (Armstrong et al., 2018), reconstruct snow water equivalent (SWE) (Guan et al., 2013; Bair et al., 2016; Rittger et al., 2016), quantify anthropogenic LAP impacts on snowmelt timing (Bair et al., 2021b, 2016), and forecast streamflow (Micheletty et al., 2021).

Fundamental to mapping snow with remote sensing is the knowledge that snow cover varies at a finer spatial scale than

the scale of the data collected by most current and upcoming spaceborne optical sensors. Thus, relevant studies require subpixel retrievals. The importance of subpixel snow is well recognized, as evidenced by the development of fSCA approaches for application to high-spatial-resolution Airborne Visible/Infrared Imaging Spectrometer (AVIRIS) data in the early 1990s and to high-resolution commercial satellite data over the past decade (Nolin and Dozier, 1993; Selkowitz et al., 2014). At a 463 m spatial resolution (i.e., the sinusoidal tile product grid cell size of Moderate Resolution Imaging Spectroradiometer (MODIS) data with a ground sample distance of 500 m at nadir) (Campagnolo and Montaña, 2014), many pixels are not fully snow-covered, even in the middle of winter (Fig. 1). Even at a 30 m spatial resolution (i.e., that of Landsat 8), 25 %–93 % of pixels in middle-latitude alpine environments are mixed pixels (Selkowitz et al., 2014). Though fully snow-covered pixels are more common in some relatively high latitude regions that contain extensive permanent snow and ice, e.g., Greenland, mixed pixels are pervasive at the boundaries of ice sheets and caps in these areas. Likewise, high-latitude boreal forests contain mixed pixels. To estimate fSCA – a critical parameter in snow and terrestrial hydrology research – subpixel snow cover estimates are needed, as snow cover properties (e.g., albedo) differ from whole-pixel properties when pixels are not fully snow-covered.

Satellites provide consistent global snow cover information, yet to date, no comprehensive validation of subpixel snow cover mapping has been conducted with independent data covering multiple snow climates. In this study, we evaluate and compare snow cover retrievals among multiple sensors and algorithms. High-spatial-resolution (3 m) snow depth data derived from airborne light detection and ranging (lidar) sensors, which can penetrate forest canopies, are used in this work to create snow cover maps to validate a suite of snow cover products.

2 Background

We focus on validating snow mapping algorithms that determine fSCA using either empirical relationships based on the normalized difference snow index (NDSI, a band ratio technique) (Salomonson and Appel, 2004) or spectral-mixture analysis (Nolin et al., 1993). Snow can be distinguished from other surfaces using NDSI (Eq. 1) (Dozier, 1989) because snow is highly absorptive (low reflectance) in the shortwave infrared (SWIR) wavelengths and highly reflective in the visible (VIS) wavelengths compared to most other land surfaces (Fig. 2):

$$\text{NDSI} = \frac{R_{\text{VIS},\lambda} - R_{\text{SWIR},\lambda}}{R_{\text{VIS},\lambda} + R_{\text{SWIR},\lambda}}, \quad (1)$$

where NDSI ranges from -1 to $+1$ and R is the reflectance for each band in the subscript. The simplicity of NDSI is appealing and explains its prevalence (Hall et al., 2002; Sa-

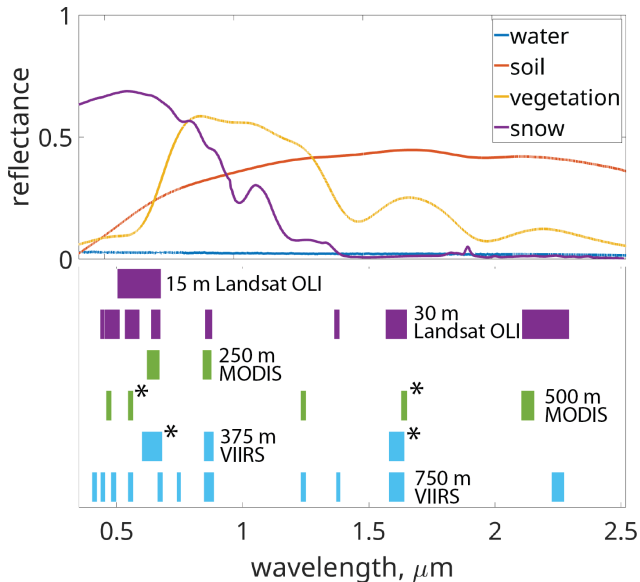


Figure 2. Hyperspectral measurements of common land surfaces: average Alfisol soil, *Pinus* vegetation, and water spectra (Meerdink et al., 2019; Baldrige et al., 2009) along with a typical dirty mountain snowpack from Mammoth Mountain, CA, on 1 May 2021. The lower panel shows the bands and spatial resolutions corresponding to the satellite sensors used in this study. The black asterisks denote the NDSI bands, while the spectral-unmixing approaches use all bands to map snow.

lomonson and Appel, 2004; Hall et al., 2010; Justice et al., 2013). However, NDSI conveys no information regarding the spectral signature of snow; various non-snow mixed pixels can yield the same NDSI values as snow-covered pixels (Stillinger et al., 2019). Additionally, NDSI is often used with a threshold to create binary snow cover maps. However, these thresholds have been shown to be both spatially and temporally nonstationary (Harer et al., 2018; Tong et al., 2020). Further, the uncertainty in these thresholds increases with an increased spatial resolution (e.g., those of Landsat satellites) and in forested areas (Klein et al., 1998). Past studies have shown that NDSI is less accurate than spectral-unmixing techniques when estimating fSCA over various terrains and at both middle and high latitudes (Rittger et al., 2013; Masson et al., 2018; Aalstad et al., 2020).

A more sophisticated and physically based method, spectral-mixture analysis, is an inversion approach derived for various surfaces; in this method, the measured reflectance is matched to a modeled reflectance to estimate the endmember fractions and surface properties (Adams et al., 1986; Roberts et al., 1998). Multiple linear equations are simultaneously solved for endmembers (Eq. 2), and $R_{s,\lambda}$ is the modeled surface reflectance at wavelength λ :

$$R_{s,\lambda} = \sum_{i=1}^N F_i R_{\lambda,i} + \varepsilon_{\lambda}, \quad (2)$$

where F_i is the fraction of endmember i ; $R_{\lambda,i}$ is the reflectance of endmember i at wavelength λ ; N is the number of endmembers; and ε_{λ} is the residual error. The model is run iteratively to minimize the root-mean-square error (RMSE) between the modeled and observed surface reflectance values. This approach was first used to estimate snow properties from hyperspectral AVIRIS airborne data (Nolin and Dozier, 1993; Nolin et al., 1993; Painter et al., 1998, 2003). The MODIS Snow-Covered Area and Grain Size (MODSCAG – or SCAG more generally) algorithm (Painter et al., 2009) proved that spectral unmixing was a viable approach to snow mapping when using multispectral satellite data. The MODSCAG algorithm can map fSCA at larger spatial scales and with more frequent temporal repeats than those possible with airborne AVIRIS-derived hyperspectral datasets. MODSCAG solves for each pixel in each image and, in addition to fSCA, also outputs fractional vegetation and fractional soil and rock information. A modified version of the SCAG algorithm (Rittger et al., 2021a) is used by the United States Geological Survey (USGS) in their fSCA Landsat product (Selkowitz et al., 2014). Developed more recently, the Snow Property Inversion from Remote Sensing (SPIReS) (Bair et al., 2021a) spectral-unmixing approach builds on the previously described spectral-unmixing efforts but uses only two endmembers (snow and snow-free) plus ideal shade to simultaneously solve for fSCA, the snow grain size, and the snow contaminant concentration. Other research-based approaches to spectral-mixture analysis have been developed for multispectral satellite data, such as the MODIS Imagery Laboratory (MODImLab) (Sirguey et al., 2009) or *SnowFrac* (Vikhamar and Solberg, 2003), but these approaches are not available for the dates or areas considered in this analysis.

Despite the long history of mapping snow from space, spatial validations of the available standard (produced operationally by an agency) products are limited. Shortly after MODIS-derived standard snow products were released in the early 2000s, researchers compared sparse subsets of individual pixels from these new standard snow products to point-scale snow depth measurements (Simic et al., 2004; Ault et al., 2006; Klein and Barnett, 2003; Maurer et al., 2003). These comparisons were followed by fSCA validations performed using relatively coarse resolution datasets, e.g., 463 m pixels compared to 250 m pixels in Hall and Riggs (2007). More extensive validations were performed for MOD10A1 binary snow cover, MOD10A1 fSCA, and MODSCAG (Rittger et al., 2013). Using 172 scenes, Rittger et al. (2013) assessed the accuracies of these products in a number of regions across the western USA and in the Himalaya by applying spectral-mixture analysis to the Landsat Enhanced Thematic Mapper Plus (ETM+) surface reflectance product at a 30 m scale. The results showed improvements resulting from using a fractional approach at 30 m compared to a binary approach, especially when performing validations in forested regions.

These past studies assessed only the viewable snow cover, i.e., the snow cover that is directly measurable from space with optical sensors during cloud-free overpasses. However, in forested regions, canopies obstruct snow cover, making validations under forest canopies difficult. Reference validation data are typically derived either from ground stations (typically representing point data in open areas) or from Landsat (limited to viewable fSCA). Recent studies have provided insights into snow cover mapping in forests using novel ground-based data and airborne lidar measurements. Raleigh et al. (2013) used gridded soil temperature networks to evaluate the MODSCAG algorithm using a static canopy adjustment method against sites exhibiting a range of canopy cover in the Sierra Nevada. Rittger et al. (2020) used the same dataset to validate a viewable snow cover to on-the-ground snow cover adjustment process involving the simultaneously retrieved pixel vegetation fraction in SCAG for pixels with canopy cover fractions up to 0.75. Bair et al. (2021a) compared MODIS- and Landsat-derived fSCA data to WorldView-2 and WorldView-3 and Airborne Snow Observatory (ASO) aerial lidar data (Painter et al., 2016) while focusing their validation on the difference between the viewable fSCA (WorldView validation) and canopy-corrected fSCA (the ground snow cover validated with aerial lidar).

While these past studies advanced validation efforts, the present study offers two notable improvements: (1) all currently available snow mapping products (including new gap-filled products) are compared across (2) a diverse range of snow climates. With the emergence of new snow mapping products and available high-spatial-resolution (i.e., meter-scale) snow depth estimates derived from aerial lidar technology, the comprehensive evaluation undertaken herein is critical.

3 Study area

Our study area comprised regions in California and Colorado in the western USA (Table 1). Validation locations were selected based on the availability of ASO (Painter et al., 2016) snow depth measurements obtained during snow-covered and snow-free flights using a lidar instrument (Sect. 4.2.1). Full-waveform lidar instruments are usually able to penetrate forest canopies, representing a significant advancement in aerial snow mapping (Deems et al., 2013a, b). Figure 3 shows the spatial extents of the validation regions and the Sturm and Liston (2021) snow type classification scheme (Sect. 4.2.4) corresponding to each region. Quantifying algorithm performance from the perspective of snow types enables a better understanding of expected performance in geographical regions without validation data or past studies. Additionally, fSCA can depend on the snow climate (Liston, 2004; Clark et al., 2011); thus, validating across various snow climates allows a range of subpixel snow distributions and depletion dy-

namics to be sampled, thereby strengthening our confidence in the global application abilities of these products.

4 Methods

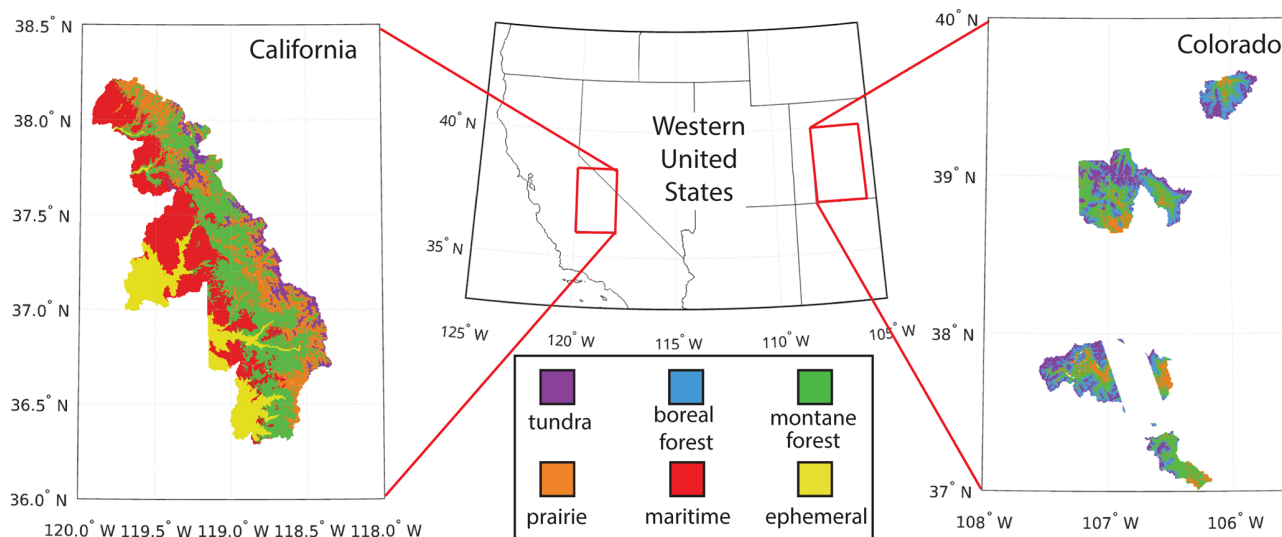
Table 2 lists the seven snow cover products evaluated against snow cover maps derived from high-resolution airborne lidar data. These products include two NDSI-based standard products, MOD10A1F and VNP10A1F, and five spectral-mixture products, the USGS Collection 1 Landsat 8 Level-3 fSCA product (USGS FSCA), the SCAG algorithm run on MODIS (STC-MODSCAG) and Landsat 8 (OLISCAG), and the SPIReS algorithm run on MODIS and Landsat 8. The daily products are all gap-filled products. All products are described in detail in individual sections below.

We selected data from all products that matched the dates of ASO flights from 2013–2020. On 20 d, an ASO flight occurred on the same day as Landsat 8 data acquisition. Three of the ASO flights corresponded with extensive thin cloud cover during the corresponding Landsat 8 overpasses (although not during the ASO overpass) and were thus removed to validate snow mapping abilities under clear skies. Other scenes contained small amounts of cloud cover. These pixels were masked and removed.

Because the MODIS and the Visible Infrared Imaging Radiometer Suite (VIIRS) products have daily temporal resolutions, corresponding MODIS/VIIRS snow cover maps are available for all ASO flight dates. ASO sometimes mapped multiple watersheds on the same day, and these products can be included within the bounds of a single MODIS/VIIRS tile. For STC-MODSCAG and MODIS SPIReS, there are 116 ASO flights. The historical records of MOD10A1F and VNP10A1F have not been processed completely (as of May 2022, the time of the analysis), so we used all currently available products, totaling 87 ASO flights for VNP10A1F and MOD10A1F. These validation data provided sufficient coverage for conducting comprehensive analyses of MOD10A1F and VNP10A1F. For MODIS and VIIRS, all validation scenes were used because all algorithms used to construct these products include temporal filters that improve the snow mapping ability based on data collected on adjacent days (a feature that no Landsat 8 product has). Including all scenes thus supported the goal of this work regarding the validation of daily gap-filled products. The standard VIIRS product, VNP10A1F, was the only VIIRS product examined. Both SCAG and SPIReS can run on VIIRS but have not yet been produced for the dates and areas considered in this study. We note that VIIRSCAG shows a nearly identical performance to that of MODSCAG (Rittger et al., 2021a).

Table 1. Watershed and snow type characteristics corresponding to each study location.

Watershed name	State	ASO flights (no.)	Watershed area (km ²)	Canopy cover	Snow class fraction					
					Tundra	Boreal forest	Maritime	Ephemeral	Prairie	Montane forest
Kings Canyon	California	13	3565	25 %	7 %	0 %	19 %	12 %	24 %	39 %
Merced River	California	8	835	20 %	6 %	0 %	55 %	2 %	15 %	21 %
San Joaquin	California	21	4234	29 %	6 %	0 %	35 %	20 %	14 %	26 %
Tuolumne River	California	34	1674	12 %	6 %	0 %	35 %	1 %	30 %	29 %
Kaweah River	California	3	1450	37 %	0 %	0 %	14 %	40 %	9 %	37 %
Lakes Basin	California	14	28	16 %	19 %	0 %	0 %	0 %	20 %	60 %
Lee Vining Creek	California	1	114	8 %	28 %	2 %	0 %	0 %	28 %	41 %
Rush Creek	California	1	139	9 %	24 %	1 %	0 %	0 %	27 %	49 %
Reds Lake	California	1	2	20 %	1 %	0 %	0 %	0 %	38 %	61 %
Blue River	Colorado	4	866	25 %	31 %	44 %	0 %	0 %	6 %	19 %
Crested Butte	Colorado	2	178	18 %	31 %	21 %	0 %	0 %	6 %	42 %
Conejos River	Colorado	1	729	27 %	13 %	16 %	0 %	0 %	13 %	58 %
Aspen/Castle-Maroon	Colorado	2	326	22 %	47 %	27 %	0 %	0 %	1 %	24 %
Gunnison-East River	Colorado	2	1670	24 %	21 %	24 %	0 %	0 %	13 %	41 %
Grand Mesa	Colorado	5	322	29 %	6 %	64 %	0 %	0 %	1 %	29 %
Gunnison-West River	Colorado	3	658	29 %	22 %	38 %	0 %	0 %	6 %	34 %
Rio Grande	Colorado	1	1862	16 %	25 %	32 %	0 %	0 %	17 %	27 %

**Figure 3.** Snow cover types present in the ASO validation flight locations. All six of the Sturm and Liston (2021) seasonal snow type classes are present in the combined California and Colorado ASO datasets.

4.1 Validated snow cover products

4.1.1 MOD10A1F

From the suite of MOD10 snow products, all of which use the same snow detection algorithm, MOD10A1F was selected; this product is the currently available gap-filled Collection 6 MODIS snow product. MOD10A1F is an NDSI-based snow cover product in which NDSI values are delivered as snow cover estimates; NDSI values below 0.1 are flagged as no snow. The product is constructed daily at a 463 m spatial resolution and undergoes gap filling to adjust for cloud cover or poor data by reusing measurements taken on the most recent clear-sky day. This product is not always spatially or tem-

porally complete as there is no backwards interpolation of snow cover if the initial days of the water year are cloud covered. However, NDSI cannot be used as a direct estimate of the fSCA value of a given pixel. In the deprecated MODIS MOD10A Collection 5 products, additional processing was conducted to convert NDSI values to fSCA values; however, these products are no longer delivered. In addition to comparing the Collection 6 NDSI snow cover information contained in MOD10A1F, we estimated fSCA using the Collection 5 MODIS Terra relationship (Eq. 3). This relationship was originally developed using Landsat data, and we assumed here that the equation parameters and formulation are still valid for the Collection 6 products (Salomonson and Appel, 2006, 2004). Notably, with the applied correction, the

Table 2. Snow cover products validated in this study and their characteristics.

Product	Resolution (temporal/spatial)	Reference	Canopy adjustment method	Minimum snow cover fraction (besides 0)	Gap-filling method	Near real time
MOD10A1F	Daily/463 m	Hall et al. (2019)	None	0.1 NDSI snow cover; 0.135 fSCA	Hall et al. (2010)	Yes
VNP10A1F	Daily/375 m	Riggs et al. (2019)	None	0.1 NDSI snow cover; 0.135 fSCA	Hall et al. (2010)	Yes
USGS FSCA	16 d/30 m	Selkowitz et al. (2017)	Spatial replacement (Selkowitz et al., 2017; Sect. 4.1.5)	0.15 fSCA	None	Yes
STC-MODSCAG	Daily/463 m	Painter et al. (2009), Rittger et al. (2020)	Rittger et al. (2020); scaled adjustment (Sect. 4.1.3)	None	Rittger et al. (2020)	Yes
OLISCAG	16 d/30 m	Rittger et al. (2021a)	Rittger et al. (2020); scaled adjustment (Sect. 4.1.4)	0.1 fSCA	None	No
SPIReS (MODIS)	Daily/463 m	Bair et al. (2021a)	Viewable gap fraction (Sect. 4.1.6)	0.1 fSCA	Bair et al. (2021a)	No
SPIReS (Landsat 8)	16 d/30 m	Bair et al. (2021a)	Scaled adjustment and spatial interpolation (Sect. 4.1.7)	0.1 fSCA	None	No

minimum possible fSCA value (besides 0) was 0.135.

$$\text{fSCA} = -0.01 + (1.45 \times \text{NDSI}) \quad (3)$$

Previous MOD10 collections included processing steps in which the normalized difference vegetation index (NDVI) was used to improve the snow detection ability in forested areas (Klein et al., 1998); however, low NDSI values should be mapped as snow using the updated fractional method (Salomonson and Appel, 2004).

4.1.2 VNP10A1F

We accessed the first version of the VIIRS standard snow product, VNP10A1F (Riggs et al., 2019); this product is nearly identical to MOD10A1F, but VIIRS obtains surface reflectance data at slightly different bandpasses and spatial resolutions (see Fig. 2). All VNP10 snow products use the same snow detection algorithm as the MOD10 products. The utilized product was a 375 m resolution daily snow product delivered as a gap-filled NDSI product. The same gap-filling approach used to construct MOD10A1F was applied to VNP10A1F. As no published adjustments are available for converting NDSI values to fSCA values, we also reused the same retrieval algorithm applied to MOD10A1F, shown in Eq. (3).

4.1.3 STC-MODSCAG

MODSCAG (Painter et al., 2009) is a spectral-mixture analysis approach that uses a library of endmembers representing clean snow reflectance, soil/rock, vegetation, and

photometric shade and performs least-squares fitting to obtain fSCA from MODIS Terra surface reflectance products (MOD09GA). In this approach, the fraction of each of the endmembers was estimated along with the snow grain size corresponding to the snow endmember for each pixel in every image. Some non-linear effects were incorporated by including canopy-level vegetation endmembers. The data were then gap-filled based on spectral and persistence filters (Rittger et al., 2020) and interpolation while preferentially weighting nadir views over off-nadir views (Dozier et al., 2008). This gap-filled product is called the spatially and temporally complete MODSCAG (STC-MODSCAG) product. Viewable fSCA, fractional vegetation (fVEG), and fractional soil/rock (fROCK) information available from MODSCAG is used for STC-MODSCAG. In STC-MODSCAG, vegetation height maps (Simard et al., 2011), viewable fSCA, and fVEG are used to estimate snow on the ground. When the viewable fSCA is greater than 0.1 in forested areas identified by a vegetation height greater than 2.5 m, fSCA is adjusted using concurrently observed fVEG. Rittger et al. (2020) showed the STC-MODSCAG canopy correction method to be a function of the view angle. Additional post-processing was conducted to increase the accuracy of the results in both forested and alpine regions. In forested areas, the maximum snow cover is limited using a vertical-to-horizontal crown radius ratio (Liu et al., 2004) to remove snow where tree trunks exist. In alpine areas (i.e., areas with vegetation heights < 2.5 m and elevation > 800 m in this analysis), the retrieved fSCA was scaled by +10 % of the initial value. The data utilized in the analyses performed in this paper

were produced by Snow Today at the National Snow and Ice Data Center (NSIDC, <https://nsidc.org/snow-today>, last access: 28 June 2022). Snow Today is supported by NSIDC Distributed Active Archive Center (DAAC) User Services and has provided freely available daily images in near real time since 2020. The historical records from earlier STC-MODSCAG versions are available via file transfer protocol (FTP) at <http://snow.ucsb.edu> (last access: 29 June 2022).

4.1.4 OLISCAG

OLISCAG uses the same spectral-mixture analysis approach as MODSCAG but applies this approach to Landsat 8 Operational Land Imager (OLI) data (Rittger et al., 2021a). The spectral libraries differ based on the number and size of bandpasses used by each instrument. The images are not interpolated temporally or spatially as is performed with the STC-MODSCAG data (described above). The SCAG model was generalized for the Landsat ETM+ and TM instruments (Rosenthal and Dozier, 1996; Painter et al., 2009; Rittger et al., 2013), and Rittger et al. (2021a) modified the SCAG algorithm to work with the new 12-bit OLI data using spectral libraries updated specifically for OLISCAG. Similarly to STC-MODSCAG, a canopy adjustment is applied to the OLISCAG viewable fSCA to obtain on-the-ground fSCA. The viewable fSCA is adjusted when a minimum fSCA is detected (0.1) using the concurrently estimated vegetation fraction and the crown ratio equation in Liu et al. (2004), which are similar to the processing methods described above for STC-MODSCAG. OLISCAG has a minimum fSCA detection threshold set at 0.1.

4.1.5 USGS Landsat fSCA

fSCA is available from the Landsat 8 Collection 1 Level-3 products provided by the USGS. The Collection 1 product is produced for the western USA and Alaska in the Landsat Analysis Ready Data tiles and is constructed through a spectral-mixture analysis based on the SCAG algorithm (Painter et al., 2009) using spectral libraries from OLISCAG (Rittger et al., 2021a). This product represents a significant advancement over the standard snow maps available in the Level 1 and 2 band quality assessment files delivered with Landsat 8 reflectance data. The SCAG implementation includes the application of snow-specific cloud masking, water masking, and canopy cover adjustments to construct the final fSCA product (Selkowitz et al., 2017). The primary difference between OLISCAG and the USGS fSCA product is in their canopy correction approaches. In the USGS fSCA product, snow cover in pixels identified as forest pixels using the National Land Cover Database (NLCD) (Homer et al., 2004) is replaced with snow cover from less forested nearby pixels with similar accumulated solar radiation and elevation. This product has a minimum fSCA detection threshold set at 0.15.

4.1.6 MODIS SPIReS

SPIReS (Bair et al., 2021a) is an open-source (see “Code and data availability”) spectral-unmixing approach designed to map fSCA using pixels from snow-free periods as background reflectance information and a modeled snow endmember that contains contaminants (e.g., dust or soot). These two endmembers are mixtures themselves, thus reducing the number of unknowns and making the system more highly overdetermined (Branham, 1990), in turn increasing the accuracy and computational speed. Additionally, the background endmember mixtures account for some pixel-specific non-linear effects, such as canopy effects. SPIReS clusters pixels within a tolerance and then simultaneously solves for fSCA, the grain size, and the contaminate concentration at the surface of the snowpack for each cluster and applies the solution to all pixels in each cluster. This process typically results in a 10–100× reduction in the number of unmixing model runs required compared to solving for every pixel. The latter two properties are then used to estimate snow albedo (Bair et al., 2019). SPIReS adjusts the viewable snow cover to account for shading, permanent ice, and snow hidden by forest canopies. Following the initial publication of the SPIReS method by Bair et al. (2021a), SPIReS was adjusted to better handle specific snow mapping situations. If a pixel is fully snow-covered, no snow-free background surfaces should be visible. SPIReS accounts for this issue by solving for pixels twice, first with the standard method including a “snow-free” background reflectance and then again with no background. If this second solution is within 2 % of the original solution, the new “no-background” solution is used. The goal of this double-solving approach is to significantly reduce the biases that arise for pixels with high fSCA values.

In MODIS SPIReS, the canopy correction step is based on the viewable gap fraction (VGF) estimated for each pixel, i.e., an estimate of the fraction of the pixel that comprises viewable ground. This fraction is a function of the canopy cover, topography, and satellite view angle. VGF adjustments are performed when constructing MODIS SPIReS to account for the satellite view angle based on the Geometrical Optical Model (Liu et al., 2004). For MODIS SPIReS, persistence filters based on both the snow cover and the minimum snow grain size alongside temporal smoothing with weighted splines (Dozier et al., 2008) are used to generate daily, gap-free snow cover and surface snow property estimates corresponding to each pixel. While Bair et al. (2021a) found through an *F*-statistic analysis that the fSCA detection abilities were maximized at 0.01 for MODIS and 0.07 for Landsat OLI, the minimum fSCA threshold for SPIReS was set to 0.1 in this study, the current default setting.

4.1.7 Landsat SPIReS

Landsat SPIReS is constructed by applying the same approach as MODIS SPIReS, with a few differences. Because Landsat is a nadir-looking push-broom instrument, the Geometrical Optical Model is not used. Instead of a VGF adjustment, for pixels with canopy cover fractions above 0.5, fSCA is ignored and spatial interpolation is used to spread snow into these pixels in which the direct snow cover measurements are unreliable. Similarly to the OLISCAG and USGS fSCA products, no gap-filling procedures (apart from the canopy correction step described above) are used to construct the Landsat SPIReS product.

4.2 Validation datasets

4.2.1 ASO snow depth

ASO produces snow depth and SWE products that are archived at NSIDC (2013–2019) and at the ASO, Inc., website (2019–present) for use by researchers and water managers (Painter et al., 2016). We obtained all available ASO data from water years 2013–2020. In this study, the 3 m snow depth products were first converted into a binary snow map and then coarsened into an fSCA product matching the spatial resolution and projection of MODIS, VIIRS, or Landsat (as described below); these fSCA products were then used to validate the satellite-derived snow products (Sect. 4.3).

The 3 m ASO snow depth data represent an intermediate ASO product without the same level of quality control as the final 50 m SWE products. The 3 m datasets are associated with extensive data representation issues; for example, “zero” is used as both a fill value and a snow-free classifier. To convert the 3 m snow depth data to high-quality 3 m snow cover maps, additional data cleaning was thus mandatory. To improve the quality of the 3 m snow depth data and to ensure the use of valid measurements, the data extent was limited to the basin boundaries and to the 3 m depth measurements co-located with valid measurements in the 50 m SWE dataset derived during the same flights. The validation datasets were cropped to the basin boundaries even when the flight lines extended past these boundaries, as the data collected outside the basin boundaries were often unreliable. At certain times late in the melt season, when snow was present only at the highest elevations in the studied basins, flights did not extend across the whole basins; under these conditions, we used the 50 m SWE datasets with snow-free, snow, and missing-value representations to select valid spatial regions from the 3 m snow depth products.

To convert the ASO snow depths to fSCA maps, the cleaned ASO-derived 3 m snow depth data were first relabeled as snow-free, snow-covered, or filled data. The mean absolute error (MAE) of the 3 m snow depth product has been reported to be less than 8 cm (Painter et al., 2016); hence, these snow depth measurements were converted into a 3 m

binary snow cover mask in which the snow cover was considered true when the snow depth was greater than 8 cm; “snow-free” areas referred to measured snow depths of 8 cm or less; and “fill” data were established where the 3 m depth product had missing data, the 50 m SWE product had missing data, or the analyzed pixels were located outside the basin boundaries. Only 1.9 % of ASO snow depths had values less than 8 cm. These binary 3 m snow cover maps were then coarsened to the same spatial resolution as each fSCA satellite product for the subsequent validation. The 3 m binary snow cover maps were coarsened via Gaussian pyramid reduction to reach the significantly coarser validation resolutions, and then bilinear interpolation was used to reproject the coarsened ASO-derived snow cover validation data to the native projection and spatial grid of each snow product. In addition to reducing geolocation issues between datasets, this coarsening method further reduced the possible influence of spurious misclassifications of thin snow as false negatives in the ASO validation dataset. Any reprojected validation pixels with fSCA values less than 0.01 were assumed to be snow-free (i.e., fSCA = 0). The goal of the chosen thresholds was to eliminate artifacts resulting from upscaling the 3 m data to coarser resolutions (i.e., 120 m for Landsat and 2 km for MODIS/VIIRS validation; Sect. 4.3.1) while comparing as many pixels as possible. False positive snow cover measurements arising due to thin snow measured within the uncertainty range of the ASO lidar data were thus effectively removed. During our analysis, we tested different thresholds, and a change in the threshold value did not significantly change the results in any meaningful way. Some previous validation efforts ignored low-snow-cover-fraction pixels (Painter et al., 2009; Rittger et al., 2013), but newer (Masson et al., 2018) studies have also examined the low snow cover fractions. ASO, like any validation source, is imperfect. ASO may not map all rock outcrops correctly in alpine regions and may instead consider those locations to be fully snow-covered. Additionally, in regions with steep terrain and dense forests, depending on the orientation of the flight line relative to the underlying surface, the lidar retrieval quality may vary. Even given these concerns, comparisons between ASO and WorldView-2 and WorldView-3 high-resolution optical imagery derived in snowy mountainous terrain have shown that ASO is a high-quality validation source (Bair et al., 2016, 2021a), and we treated these data as validation truth in this paper.

4.2.2 Canopy cover

The static NLCD 2016 tree canopy cover dataset (Wickham et al., 2021) with a 30 m spatial resolution was used to determine the canopy cover locations and fractions (0–1) within the validation regions. NLCD 2016 uses spectral and geographical information to determine land cover types and was chosen due to its operational availability and 30 m spatial resolution. These NLCD canopy cover files were cropped and

stored with the ASO dataset representing the corresponding day and then reprojected alongside the ASO validation datasets to the native projection and resolution of each product. These coarsened canopy cover maps were then used to categorize pixels into canopy cover bins for the subsequent statistical analysis across the full range of existing canopy cover fractions in the study areas.

4.2.3 View angle

MODIS and VIIRS are both scanning whisk-broom sensors that have sufficiently wide fields of view with variations in the sizes of individual pixels across a given swath (Dozier et al., 2008). In addition to these pixel size variations, off-nadir views, especially those obtained in pixels with canopy cover, cause variations in the fraction of the surface under the canopy that is visible to the satellite in each pixel (Rittger et al., 2020; Bair et al., 2021a). For both MODIS and VIIRS, NDSI-based approaches do not adjust for the view angle, whereas the SCAG and SPIReS approaches do account for the view angle (see above). To understand how well these algorithms map snow cover when high-view-angle acquisitions have occurred, we took the per-pixel satellite view zenith angle information from the top layer in the MOD09GA or VNP09GA surface reflectance product corresponding to the date and location of the target snow cover estimate and binned the derived statistical results by the viewing geometry in 5° bins ranging from 0° (nadir) to 70° (edge of scan). As Landsat carries a push-broom sensor, it acquires near-nadir images across all pixels, so no view angle analyses were performed for the Landsat 8 datasets.

4.2.4 Global seasonal snow classifications

The study area considered herein was classified into seasonal snow cover types using the Sturm and Liston (2021) classification scheme, which includes six snow categories (tundra, boreal forest, maritime, ephemeral, prairie, and montane forest snow) on a 1 km global classification map. These data are available at the NSIDC website (<https://nsidc.org/data/NSIDC-0768/versions/1>, last access: 3 January 2022). For each product, the derived error statistics were binned into the snow class corresponding to each fSCA pixel using a nearest-neighbor resampling approach.

4.3 Validation

4.3.1 Upscaling

In the validation process, the ground-truth snow cover maps derived from ASO were compared to each fSCA product. The abilities of each algorithm to detect snow (Sect. 4.3.2) and correctly estimate the fSCA values in each pixel and in each watershed basin (Sect. 4.3.3) were evaluated separately. To account for geolocational uncertainty in the satellite products, we upscaled the fSCA values obtained from each prod-

uct before the validation. The Landsat 8 products were validated at a 120 m spatial resolution, and the MODIS/VIIRS products were validated at a 2 km spatial resolution. Both the ASO validation data and the satellite data were coarsened to the spatial resolution and original projection of the corresponding satellite products. This same approach has been adopted in past validation studies in which snow products were compared to relatively high spatial resolution validation data (Stillinger et al., 2019; Bair et al., 2021a, 2016; Rittger et al., 2013, 2020). While VIIRS data are available at a 375 m spatial resolution compared to the 463 m resolution of MODIS data, both products were validated herein at a 2 km spatial resolution. Each product is validated as it is delivered to users; thus, no additional thresholds were applied to set a minimum snow cover.

4.3.2 Snow detection

To validate the snow detection results, a binary mask of ASO-derived snow cover (ASO fSCA > 0) was compared to binary masks of the product-derived snow cover (product fSCA > 0), and snow cover was considered a true positive (TP) in all cases where fSCA > 0. Four pixel classes were generated from the comparison: TPs, false positives (FPs), true negatives (TNs), and false negatives (FNs). TNs and, subsequently, the commonly used “accuracy” statistic that includes TNs were not used in the subsequent validation assessments as they can skew the results when large swaths of easily classified snow-free areas exist in an image. From the remaining three pixel classes (TPs, FPs, and FNs), the precision, recall, and F -statistic values were calculated (Eqs. 4, 5, and 6).

$$\text{Precision} = \frac{\text{TP}}{\text{TP} + \text{FP}} \quad (4)$$

$$\text{Recall} = \frac{\text{TP}}{\text{TP} + \text{FN}} \quad (5)$$

$$F = \frac{(2 \times \text{precision} \times \text{recall})}{(\text{precision} + \text{recall})} \quad (6)$$

Precision is a measure of how few FPs a product generates, characterizing the ability of an algorithm to include only snow in its snow classification results. A high precision of 99 % means that 99 % of the pixels mapped as snow were actually snow-covered according to the ground-truth data. Recall is a measure of how few FNs a product generates, characterizing the ability of the algorithm to map all the snow in an image. A high recall of 99 % means that 99 % of the snow-covered pixels in an image were included in the snow mask produced by the algorithm. The F statistic, the harmonic mean of precision and recall, is a way to balance these two independent algorithm performance metrics and ranges from 0 % to 100 %, as do precision and recall. A high F statistic means that the algorithm correctly mapped the snow in an image and did not include other land surface types in the produced snow maps.

4.3.3 Per-pixel and per-basin fSCA

The upscaled ASO fractional snow cover validation data discussed in Sect. 4.3.1 were compared to the fSCA estimates obtained from each product at the given validation-step spatial resolution. The evaluation approach described in Sect. 4.3.2 provides a measure of the snow detection ability of an algorithm but does not measure the ability of the algorithm to correctly estimate fSCA in a pixel. A product-derived fSCA estimate of 0.2 compared to a true fSCA estimate of 0.95 would result in a TP snow detection but would suggest a large bias and error in terms of the accuracy of the fSCA estimate. To determine how accurate the analyzed algorithms are in terms of their produced fSCA estimates, the bias and RMSE values were calculated to evaluate how well each product performed when estimating fSCA at both the pixel and basin scales. Bias is the average overall difference in the fractional snow cover estimate between a product and the ASO snow cover fraction truth map at the analysis resolution. RMSE is a measure of the average error in individual-pixel fractional snow cover estimates compared to the ASO snow cover fraction truth map at the analysis resolution.

The hydrological boundaries of basins were used when planning the ASO flights from which validation data were collected; assessing the snow cover mapping performance at this scale enables us to evaluate the ability of each product to calculate the total fSCA of a watershed. At the basin scale, the snow fractions of all validation pixels (TPs, FPs, FNs) in each basin were calculated for each product and the ASO snow cover truth map by summing the per-pixel fractional cover estimates and dividing by the number of validation pixels. The snow products were then compared to the same measurement calculated from the ASO data. The basin-wide product and ASO-derived, basin-scale fSCA were compared in each basin on each day. Past error analyses have focused on per-pixel errors, which can be used to improve confidence when fSCA data are used for high-resolution, spatially explicit models working to better understand processes. The new basin-wide error estimates derived herein provide information for larger-scale, coarser models like those used in global and regional climate simulations.

4.3.4 Specific pixel subcategories

Understanding the snow mapping performances of various algorithms under specific conditions is crucial for building confidence in algorithm quality and providing insight into scenarios that require further development to improve snow mapping abilities. In this work, the pixels in each product were separated into categories, and the statistics derived across gradients in each category were evaluated. The pixels in the Landsat 8 and MODIS/VIIRS datasets were grouped by seasonal snow class and canopy cover fraction, and the MODIS/VIIRS dataset pixels were additionally grouped by satellite view angle. Additionally, visual representations of

the error patterns were generated (see Fig. 6) by mapping the combination of the per-pixel snow cover bias from -99% to $+99\%$ alongside the TNs, replacing the -100% bias measurements with FNs and replacing the $+100\%$ bias measurements with FPs. These errors, when displayed alongside ASO fSCA maps (representing the truth) and canopy cover maps, help deliver insights into the performances of the analyzed algorithms.

5 Results

5.1 Overall statistical assessment

Table 3 highlights the results obtained from the snow detection validation analysis performed while applying the ASO data as the truth dataset. The per-pixel fSCA and basin-wide fSCA results were assessed for each product in terms of the bias, RMSE, precision, recall, and F -statistic metrics. The per-scene median, minimum, and maximum values corresponding to each statistical measure and to each product are listed in Table 3. Notably, the minimum bias and minimum recall statistics for a single product can be obtained on two different dates.

The STC-MODSCAG, OLISCAG, USGS fSCA, SPIReS Landsat, and SPIReS MODIS products all had median biases of $\sim 0\%$. The standard snow mapping products from MOD10 and VNP10 had biases of -7.1% and -9.5% , respectively, but these biases were reduced to $+2.8\%$ and -2.7% when the Collection 5 fractional snow cover correction (Eq. 3) was applied to the standard Collection 6 products, a step not taken in the archived data at NSIDC. When multiple products have no bias, the product with the lower RMSE can be considered the better-performing product. The median RMSE values (Table 3) derived herein ranged from 11.4% (OLISCAG) to 19% (VNP10AF).

The precision, recall, and F -statistic metrics measure the ability of the analyzed products to detect snow cover (Table 3). The median precision values derived herein ranged from 89.4% (VNP10AF) to 99.4% (SPIReS Landsat). In this work, the median recall values ranged from 96.2% (MOD10AF) to 100% (SPIReS MODIS and STC-MODSCAG). For Landsat products, the F statistic ranged from 97.3% (USGS) to 99.1% (SPIReS Landsat and OLISCAG), while for MODIS and VIIRS, the F statistics were lower, ranging from 93.1% (VNP10AF) to 96.1% (SPIReS MODIS). For all snow cover detection measures, the algorithm performances associated with the worst scene exhibited wide variabilities; the minimum F -statistic values ranged from 83.2% (USGS fSCA) to 0% (VNP10AF).

The basin-wide fSCA RMSE and bias validation results are presented at the bottom of Table 3. OLISCAG, USGS Landsat, SPIReS Landsat, and SPIReS MODIS had overall basin-wide biases of $\sim 0\%$. The standard NDSI snow cover products (MOD10AF and VNP10AF) had higher overall

Table 3. Snow cover fraction product validation statistics obtained for all products assessed in this study along with the total and median per-scene counts of validation pixels at the validation resolution (120 m for Landsat, 2 km for MODIS/VIIRS) of each product. Note “FSC” denotes where Eq. (3) was used to estimate fSCA from the operational NDSI products.

	Landsat 8				MODIS				VIIRS		
	SPiReS	OLiSCAG	USGS	SPiReS	STC-MODSCAG	MODi0A1F	MODi0A1F_FSC	VNPi0A1F	VNPi0A1F	VNPi0A1F_FSC	
Per-scene median	Bias	0.004	-0.004	0.003	-0.001	-0.071	0.028	-0.095	-0.027		
	RMSE	0.124	0.114	0.158	0.120	0.127	0.137	0.186	0.157		
	Precision	0.994	0.992	0.963	0.942	0.962	0.962	0.894	0.894		
	Recall	0.994	0.994	0.990	1.000	0.962	0.962	0.995	0.995		
	<i>F</i> statistic	0.991	0.991	0.973	0.956	0.944	0.944	0.931	0.931		
Per-scene maximum	Bias	0.082	0.107	0.170	0.191	0.065	0.234	0.055	0.186		
	RMSE	0.308	0.252	0.309	0.260	0.473	0.333	0.425	0.325		
	Precision	1.000	1.000	1.000	1.000	1.000	1.000	1.000	1.000		
	Recall	1.000	1.000	1.000	1.000	1.000	1.000	1.000	1.000		
	<i>F</i> statistic	1.000	1.000	1.000	1.000	1.000	1.000	1.000	1.000		
Per-scene minimum	Bias	-0.089	-0.119	-0.086	-0.159	-0.445	-0.252	-0.383	-0.216		
	RMSE	0.039	0.090	0.096	0.021	0.023	0.021	0.012	0.012		
	Precision	0.770	0.704	0.762	0.300	0.333	0.333	0.000	0.000		
	Recall	0.818	0.949	0.917	0.750	0.125	0.125	0.000	0.000		
	<i>F</i> statistic	0.829	0.815	0.832	0.429	0.182	0.182	0.000	0.000		
Basin-wide	Bias	0.004	-0.002	0.004	0.000	-0.092	0.015	-0.119	-0.035		
	RMSE	0.047	0.061	0.062	0.065	0.125	0.085	0.150	0.083		
Validation pixel counts*	Total	326 256	323 843	314 745	19 622	14 492	14 492	16 600	16 600		
	Median	8535	8553	10 380	154	138	138	177	177		

* Slight differences in pixel counts are possible due to differences in TNs among products and the MODi0/VNPi0 data availability (Sect. 4).

biases of -9.2% and -11.9% , respectively. The RMSE values obtained at the per-pixel scale were lower than those obtained at the per-pixel scale, as the overestimates and underestimates balanced each other out in the basin-wide summation. The median RMSE values derived at the basin scale ranged from 4.7% (SPIReS Landsat) to 15% (VNP101AF).

When the Collection 6 MOD10A1F and Collection 1 VNP10A1F NDSI snow cover products were corrected with the Collection 5 fractional cover linear correction (Eq. 3), the precision, recall, and F -statistic metrics were unchanged as the snow detection ability was unchanged, but the bias and RMSE values improved for both products at the per-pixel and basin scales as the fractional values were adjusted by the linear equation. All spectral-unmixing methods showed comparable snow-identification performances (i.e., similar precision, recall, and F -statistic values) across the satellite platforms and outperformed the NDSI products. The per-pixel bias and RMSE values were comparable among all Landsat 8 products. Among the MODIS products, SPIReS and STC-MODSCAG exhibited lower median bias ($\sim 0\%$) and RMSE (12%) values than the standard MOD10A1F product.

5.2 Product performances under specific conditions

In addition to the overall statistical assessment, the ability of each product to map snow under specific conditions was assessed. Figures 4 and 5 and Table 4 display the results obtained when the validation datasets were classified by canopy cover fraction, snow cover fraction, satellite view angle, and snow class. Figure 6 displays how error images were generated to highlight the spatial performance patterns at the basin scale. There were a different number of samples in each discretized bin of the four assessment categories, and the data distributions varied among the Landsat 8 products and MODIS/VIIRS products. All snow classes were represented in the MODIS data, with the lowest number of pixels available for the ephemeral snow class. No ephemeral snow class pixels corresponded to snow in the Landsat 8 validation dataset. The VNP101AF product was not available for the dates on which ephemeral snow was mapped by MODIS. The view angle analysis was performed only for MODIS and VIIRS, as Landsat acquires only near-nadir observations. In this study, our sample of snow pixels was representative of all possible MODIS and VIIRS view angles. All snow cover fractions were present in all products. There were a sufficient number of data points available across all snow cover classes to calculate error statistics across the full range of snow cover fractions. Snow cover fractions lower than the minimum snow cover fractions employed by a product (Table 2) were possible because the product and validation datasets were coarsened to account for geolocational uncertainties, and adjacent pixels with no snow cover could be included in this coarsening procedure. The snow cover distributions obtained for Landsat and MODIS/VIIRS were similar.

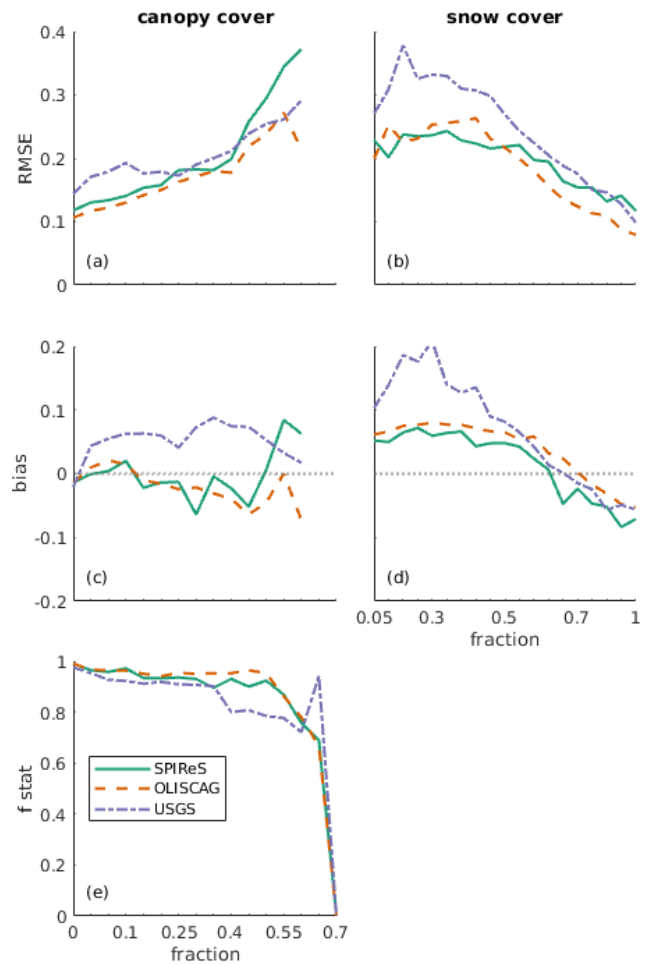


Figure 4. Snow cover mapping statistics: RMSE (a, b), bias (c, d), and F -statistic (e) values calculated for pixels binned by canopy cover fraction (a, c, e) and by ASO-derived snow cover fraction (b, d) from Landsat 8 fractional snow cover products (SPIReS, USGS, and OLISCAG). No F -statistic graph is displayed for the snow-covered area due to the low F -statistic variability associated with the snow cover fraction.

The canopy cover distributions differed between the MODIS/VIIRS and Landsat products. The Landsat products contained significant numbers of canopy-free pixels. The relatively coarse spatial resolution daily products from MODIS and VIIRS blended canopy-free with canopy-covered areas, thus reducing the number of canopy-free pixels relative to those in the Landsat products. Very few or no data points were available for the highest possible canopy cover fractions. In the MODIS/VIIRS dataset, only 3 pixels corresponded to canopy cover fractions above 0.7, so the subsequent analysis was constrained to canopy cover fractions of 0.7 and lower. For the Landsat analysis, only 380 pixels exhibited canopy cover fractions above 0.7. These pixels were used to calculate the F statistic for the Landsat product under high-canopy-cover conditions; however, due to the poor detection ability (Fig. 4e), the bias and RMSE measures were

Table 4. Heat maps of the algorithm performance results (colored by RMSE, bias, and F statistic) corresponding to seasonal snow cover types. The Landsat algorithms are denoted in the first three rows. The black boxes indicate instances of insufficient validation data.

	RMSE					bias					f stat							
USGS	0.142	0.118	0.214		0.168	0.180	-0.057	0.016	0.046		0.017	0.063	0.999	1.000	0.918		0.978	0.937
OLISCAG	0.105	0.086	0.140		0.111	0.148	-0.027	0.000	0.000		0.000	-0.031	0.999	0.998	0.945		0.987	0.981
L8 SPIReS	0.124	0.069	0.160		0.120	0.162	-0.025	-0.020	0.015		0.000	-0.031	0.999	0.999	0.944		0.988	0.953
MOD10	0.127	0.184	0.126	0.028	0.115	0.095	-0.088	-0.093	-0.057	0.000	-0.073	-0.045	1.000	1.000	0.882	0.667	0.996	0.932
MOD10-FSC	0.126	0.061	0.135	0.049	0.128	0.113	0.060	0.000	0.000	0.000	0.053	0.000	1.000	1.000	0.882	0.667	0.996	0.932
VNP10	0.230	0.202	0.190		0.166	0.130	-0.166	-0.158	-0.103		-0.107	-0.059	1.000	1.000	0.850		0.989	0.922
VNP10-FSC	0.167	0.081	0.162		0.130	0.122	-0.051	-0.044	-0.033		0.000	0.000	1.000	1.000	0.850		0.989	0.922
STC-MODSCAG	0.097	0.091	0.128	0.053	0.113	0.119	-0.017	0.000	0.000	0.000	0.000	0.000	1.000	1.000	0.925	0.667	1.000	0.969
MODIS SPIReS	0.105	0.107	0.123	0.048	0.089	0.106	-0.016	0.000	0.000	0.010	0.000	0.000	1.000	1.000	0.927	0.667	1.000	0.965
	tundra	boreal forest	maritime	ephemeral	prairie	montane forest	tundra	boreal forest	maritime	ephemeral	prairie	montane forest	tundra	boreal forest	maritime	ephemeral	prairie	montane forest

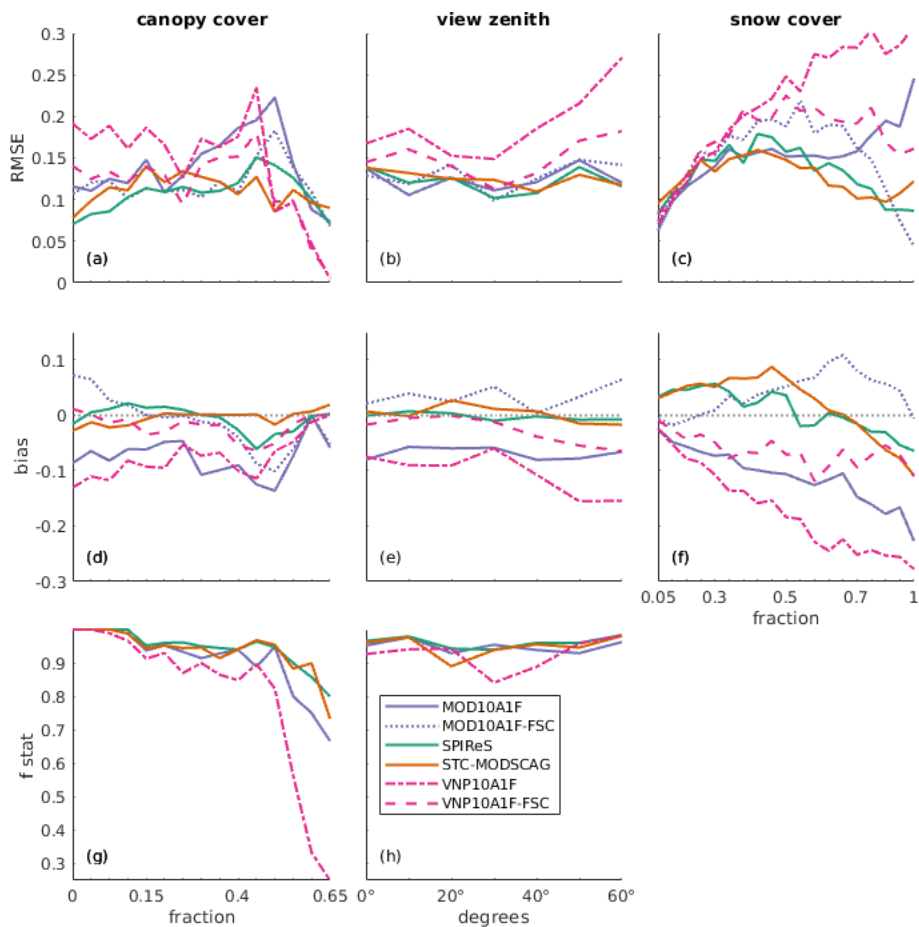


Figure 5. Snow cover mapping statistics: RMSE (a–c), bias (d–f), and F -statistic (g, h) values calculated for pixels binned by canopy cover fraction (a, d, g), view angle (b, e, h), and snow cover fraction (c, f) using the MODIS and VIIRS snow cover products. The standard products (MOD10 and VNP10) are colored so that each standard product is shown as a solid line, while the fSCA correction is shown in the same color with a dashed line (the F statistic is unchanged by the correction process). No F -statistic graph is displayed for the snow cover fraction due to the low variability in the F statistic induced by the snow cover fraction.

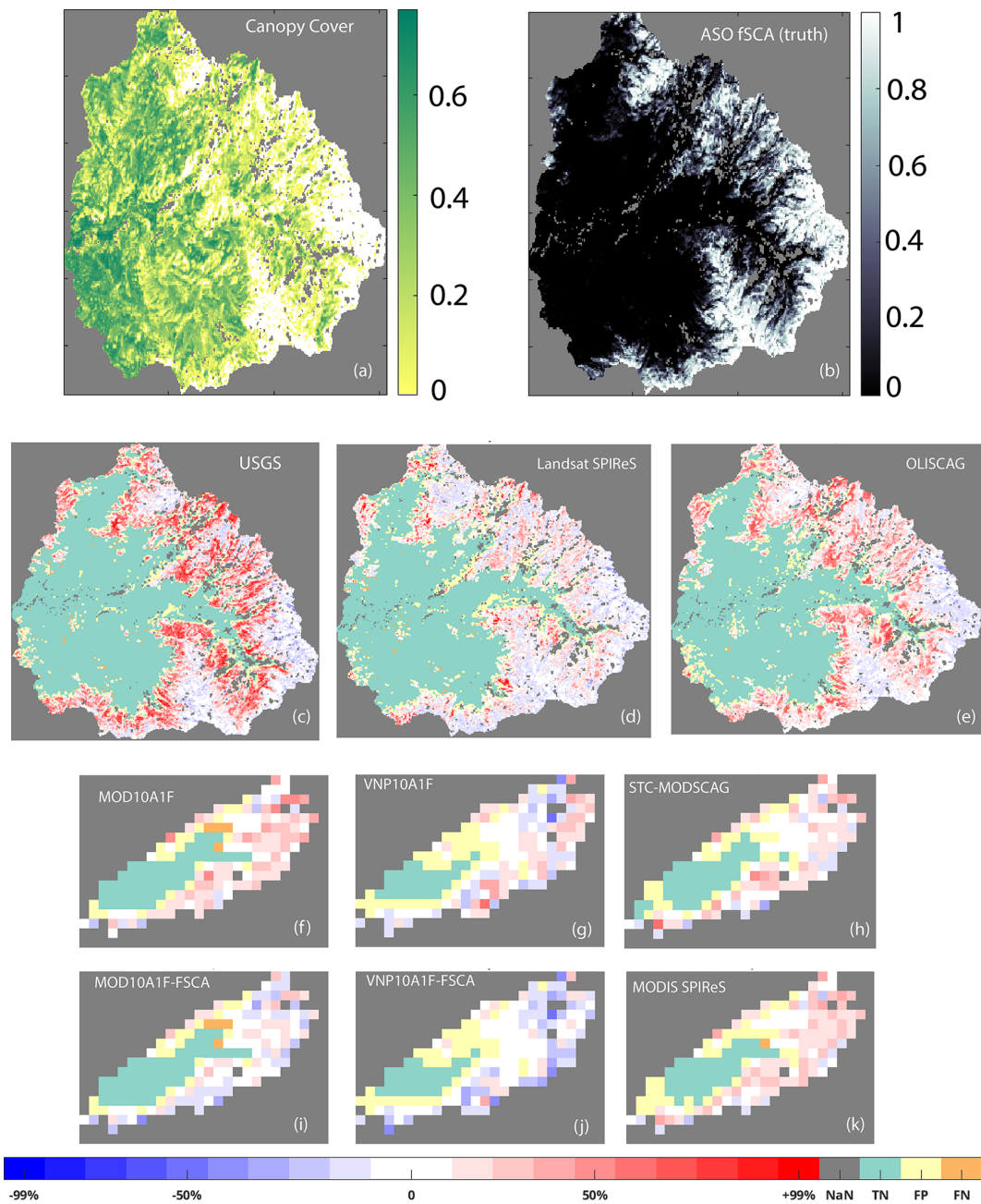


Figure 6. Merced River watershed, Sierra Nevada, California, on 7 May 2020; Yosemite Valley is approximately in the middle of these images displaying the 835 km² watershed. Panel (a) shows the canopy cover fraction. Panel (b) shows the fSCA information obtained from ASO at a 120 m pixel resolution. Panels (c)–(e) show comparisons of the Landsat products against the reference snow cover data from ASO at a 120 m pixel resolution. Panels (f)–(k) display comparisons of the MODIS/VIIRS products at a 2 km pixel resolution. The red, white, and blue pixels indicate locations where a product accurately detected snow cover (TP) but, compared to the ASO truth data, was found to have generated a positively biased result (red), an unbiased result (white), or a negatively biased result (blue). The orange pixels denote FNs (omission errors) in which the product did not correctly detect snow in the indicated location, while yellow pixels indicate FPs (commission errors) in which the algorithm incorrectly identified the presence of snow cover compared to the ASO truth dataset. The gray pixels (not-a-number (NaN) cells, outside the Merced basin) and green pixels (TNs) were not included in the analysis or used in any of the error statistic calculations performed in this paper. Note that the spatial projections differ (UTM for Landsat 8 vs. sinusoidal for MODIS and VIIRS) among the products in the panels, but all panels display the same area.

not reliable, nor were they representative of the snow fraction mapping capability of this product under such high canopy cover conditions. The bias and RMSE statistics were constrained to pixels with canopy cover fractions below 0.65, where the products could reliably detect per-pixel snow fractions.

Because the pixel distributions were not consistent across all of the analyzed categories, the statistical results obtained in this section were not directly comparable to the overall results presented in Table 3. Most pixels were found to be highly snow-covered, with minimal forest canopies; thus, this pixel type represented a relatively large fraction in the validation dataset applied in the overall validation step, the results of which are listed in Table 3. In this section, we aim to understand how well the assessed algorithms perform in specific situations that may not be representative of their overall performances but are still important for understanding their capabilities and limitations.

Figure 4 displays the snow mapping performances of all Landsat 8 products, showing similar trends associated with the canopy cover and snow cover fractions. All products obtained relatively high RMSE values under dense canopy cover conditions. The OLISCAG and SPIReS Landsat products exhibited similar RMSE trends associated with canopy cover fractions up to 0.5, while the USGS product showed relatively high RMSEs at low canopy cover fractions (Fig. 4a). The USGS product showed positive biases across all canopy cover conditions (Fig. 4b). OLISCAG and SPIReS Landsat products not only were relatively unbiased and maintained zero biases under denser canopy cover conditions than USGS fSCA but also exhibited positive and negative biases, respectively, at the highest canopy cover fractions (Fig. 4c). We found that no method utilizing Landsat data could reliably map snow cover at the highest canopy cover fractions available in this study; this finding was clearly shown by the F statistic decreasing to near zero as the canopy cover increased to 0.7 (Fig. 4e).

The products all exhibited relatively high RMSE values at the lowest snow cover fractions (Fig. 4b). All three products showed similar declining RMSE trends at high snow cover fractions, but the USGS product had higher RMSE values by approximately 5%–15% at low snow cover fractions. All three products exhibited similar but offset bias trends as the snow cover fraction increased; however, the USGS product had relatively high biases at fSCA values from 0 to 0.6 (Fig. 4d). All products overestimated the snow cover fractions corresponding to pixels with relatively low snow cover fractions and underestimated the snow cover fractions corresponding to the pixels with the highest snow cover fractions.

More variability was observed between the MODIS and VIIRS algorithm performances (Fig. 5) than among the Landsat 8 products. In the canopy cover analysis (Fig. 5a), SPIReS had the lowest RMSE when no canopy cover was present and at canopy cover fractions up to approximately 0.2, with similar errors observed across the 0.2 to 0.45 range.

STC-MODSCAG exhibited a similar but slightly worse performance up to a canopy cover fraction of 0.35 but performed slightly better at fractions from 0.35 to 0.55, when both SPIReS and VNP10 produced lower RMSE values. SPIReS and STC-MODSCAG showed the lowest biases among the analyzed canopy cover range, while the standard MODIS and VIIRS products exhibited consistent negative biases of approximately -10% under all but the densest canopy cover conditions (Fig. 5d). The snow detection ability was poor at the highest canopy cover fractions (i.e., > 0.65), so the RMSE and bias results were less reliable and are not shown. The VNP10 snow detection performance dropped off the most under dense canopy cover conditions, with MOD10, SPIReS, and STC-MODSCAG all showing similar performances as the canopy cover fraction increased (Fig. 5g).

The satellite view angle analysis results showed that the RMSE values of the snow fraction estimates were consistent among all products (except VNP10A1F) and among all view angles. For VNP10A1F, the high RMSE values derived at high viewing angles were significantly reduced when the Collection 5 linear correction was applied (Fig. 5b). The Collection 6 MOD10 and Collection 1 VNP10 products showed consistent negative biases across all viewing angles, but these biases were greatly reduced with the implementation of the Collection 5 linear correction step (Fig. 5e). The snow detection ability (i.e., F statistic) was generally unaffected by the satellite viewing angle (Fig. 5h).

The statistical analysis examining algorithm performances across the range of pixel-scale snow cover fractions showed that, overall, STC-MODSCAG and SPIReS had lower RMSE values and less bias than the standard products (MOD10 and VNP10) (Fig. 5c and f). At the highest snow cover fractions, the RMSE values obtained for the VNP10 and MOD10 products were high, in the 0.15–0.30 range, and the negative biases were large, in the -0.15 to -0.25 range (Fig. 5c and f).

All algorithms were compared to each other in terms of their performances using the global snow classification scheme shown in Table 4. Maritime snow corresponded to the largest RMSE values across all products, whereas boreal forest snow had the lowest RMSE values overall, apart from ephemeral snow regions where data were not available for all products. SPIReS Landsat, SPIReS MODIS, OLISCAG, and STC-MODSCAG consistently produced small biases across all snow types, with OLISCAG outperforming SPIReS Landsat, while the performances of SPIReS MODIS and STC-MODSCAG were virtually identical. The snow detection ability (i.e., F statistic) was high (> 0.98) among all products for tundra, boreal forest, and prairie snow, but the products performed worse for maritime, ephemeral, and montane forest snow. The spectral-mixture methods outperformed the NDSI-based methods in these challenging areas.

6 Discussion

NDSI snow cover mapping algorithms and spectral-mixture analysis models designed for use with Landsat, MODIS, and VIIRS products were validated using snow cover maps derived from all available ASO snow depth measurements collected in California and Colorado over water years 2013–2020. The spatial extent of these ASO validation data enabled the snow mapping algorithms to be validated over a wide range of conditions. Our insights extended past the overall algorithm performances to explore how well the analyzed products perform in specific situations in which accurate snow cover mapping is important but systematic biases or errors may emerge; these situations included considerations of the canopy cover conditions, per-pixel fractional snow cover, satellite view angle, and global snow type classification. In addition, we qualitatively assessed the overall spatial snow cover patterns at the river-basin scale.

Landsat data have traditionally been used in spatial validations of MODIS snow products (Rittger et al., 2013; Hall and Riggs, 2007) or for calibration tasks (Salomonson and Appel, 2004, 2006). In this study, we showed that while Landsat data have generally high snow detection and fSCA mapping capabilities, they are imperfect and do not show the same patterns as the coarser-spatial-resolution MODIS and VIIRS products. The RMSE and bias values decreased as the snow cover fraction increased for all Landsat products. The RMSE values increased and the F statistics decreased as the canopy cover density increased. Thus, for these important pixel categories, Landsat products are an imperfect measure of the fractional snow cover on the ground, while aerial lidar-based approaches can deliver improved satellite product validations.

6.1 Comparison between standard products and spectral-mixing methods

Many users rely on standard snow cover products. For Landsat 8, the USGS Collection 1 canopy-corrected fractional snow cover product exhibited a slightly worse performance than OLISCAG and SPIReS across snow cover types (Table 4) and across the analyzed canopy cover and snow cover ranges (Fig. 4). The largest difference between this standard product and OLISCAG or SPIReS was the bias metric, as neither OLISCAG nor SPIReS produced significant overall biases when mapping the snow cover fraction. The USGS Collection 1 product is available only as a canopy-corrected version over the western USA and Alaska. However, the USGS Collection 2 product expands to include a viewable snow cover product and covers the northern portion of the USA and the Aleutian Islands. Both OLISCAG and SPIReS can be run for any region globally. While OLISCAG will be released publicly in 2024 pending a processing transfer to the NSIDC DAAC, the SPIReS algorithm is currently open-source (<https://github.com/edwardbair/SPIReS>, last ac-

cess: 29 June 2022) and a viable alternative for creating high-quality snow cover fraction maps globally.

While STC-MODSCAG is produced operationally for the western USA and the Indus River basin (Rittger and Raleigh, 2022), the standard NASA global MODIS and VIIRS snow products (MOD10 and VNP10) no longer output fractional snow cover data, as NDSI values are produced instead. The results of this study suggest that the standard (NDSI-based) MODIS and VIIRS products should not be interpreted as fractional snow cover estimates. We found the now-decommissioned Collection 5 linear correction method to be effective for improving the quality of these standard products across all metrics for which they were assessed, though spectral-mixture approaches performed better in every metric assessed. The results obtained in this study support the application of the Collection 5 conversion of NDSI to fSCA (Eq. 3) in the Collection 6 standard snow products derived from MODIS or VIIRS. This conversion method does not seem to consistently cause large errors, even when applied to VNP101AF, for which this correction was not designed. A VIIRS-specific correction method may yield further improvements to the VIIRS products, as VNP10A1F performed worst across all metrics assessed in this study.

The poor performance of the VIIRS product may have stemmed from the different bandpasses used by VIIRS to calculate NDSI compared to the MODIS-utilized bandpasses (Fig. 2). The VIIRS visible band is centered on a relatively long wavelength compared to the MODIS visible band, and snow reflectance is impacted by both the fraction of the pixel covered by snow and the grain size of the snow, thus supporting simultaneous solutions for the snow fraction and grain size, as is performed with spectral-mixture approaches. A significant limitation to NDSI methods is their need to be recalibrated to achieve relative accuracy when new sensors are introduced. The VIIRS recall and precision metrics, which were unaffected by the linear correction applied to the snow cover fraction, were worse than the corresponding SPIReS MODIS and STC-MODSCAG values. Newer spectral-mixture analysis methods consistently performed as well as or better than the standard MODIS and Landsat products across all measures considered in this study. Spectral-unmixing approaches have already been shown to be robust when transitioning between sensors like MODIS and VIIRS (Rittger et al., 2021a). Based on this work, we expect SPIReS to have similar performances on VIIRS and expect these spectral-unmixing algorithms to be insensitive to bandpass differences among other sensors such as Sentinel-2a and Sentinel-2b (Bair et al., 2022) and the upcoming Thermal InfraRed Imaging Satellite for High-resolution Natural Resource Assessment (TRISHNA) mission. Global standard MODSCAG and VIIRSCAG products are currently being developed by the NSIDC DAAC, and SPIReS MODIS will be produced operationally for North America, Greenland, and High-Mountain Asia as part of Snow Today at NSIDC (Rittger and Raleigh, 2022).

6.2 Snow class insights

Mountainous regions contain some of the most diverse assemblages of snow classes among any biome around the world. In this work, we assumed that the snow class mapping performance of each product exhibited in our validation scenes was similar to the expected performance of the corresponding algorithm when assessing the same snow classes in different geographical regions. This logic enables us to use this validation method to assess algorithm performances in other global regions where high-quality, high-spatial-resolution validation data (e.g., airborne lidar-derived snow depths) are not available.

Across all snow types, the spectral-unmixing approaches SCAG and SPIReS performed as well as or better than the standard products currently available to global users. This finding gives credence to the assertion that spectral unmixing is a viable approach for mapping snow globally and that this method can improve our ability to map numerous seasonal snow cover types at the global scale. In prior decades, the computational requirements associated with spectral unmixing were seen as a barrier to operationalizing the methods into global products. Recent improvements in computing power and significant advances in algorithms have reduced the number of calculations required by 10–100× (Bair et al., 2021a), thus furthering spectral-mixture analysis methods to a point where it is no longer a barrier to run these algorithms on global datasets.

For all products assessed in this work, detecting snow (see F -statistic results) was most challenging in relatively warm, forested areas (e.g., montane forest and maritime regions). For the Landsat products, the RMSE values were highest for forested snow types. Ephemeral snow and forest snow were the most challenging snow types to detect (based on the F -statistic results). Because of the internal fSCA detection thresholds established for some products, it was difficult to map low-fSCA ephemeral snow. The assessed spectral-unmixing approaches, apart from STC-MODSCAG, do not map snow at the lowest fSCA values (Table 2) because the probability of obtaining FP detections characterized by bright non-snow surfaces increases substantially at very low (< 0.08–0.1) fSCA values. FPs create the need for persistence filters, thus hindering the ability of these algorithms to map ephemeral snow. Ephemeral snow was also the least-represented snow cover type in our analysis, and additional investigations are needed to better characterize ephemeral snow mapping capabilities involving multispectral satellites. Geostationary satellites such as the Geostationary Operational Environmental Satellite R series (GOES-R), Himawari, or Korean Multi-purpose Satellite (KompSAT) provide better temporal sampling for ephemeral snow detection than the once-daily detection abilities of polar-orbiting satellites. However, the snow mapping approach utilized by the National Oceanic and Atmospheric Administration (NOAA), while technically an application of spectral-

mixture analysis, uses only a single band and a background endmember (Romanov et al., 2003). In forests, we observed significant declines in the performances of all algorithms compared to their snow mapping abilities observed when the satellites had a clear view of the ground from space.

6.3 Canopy cover insights

This study augments prior evaluations of satellite-based snow mapping performances under dense canopy cover. STC-MODSCAG was validated under a dense canopy by Rittger et al. (2020) and Raleigh et al. (2013) with ground-based temperature sensors. While those studies considered fewer study sites than were assessed herein, their evaluations were more temporally continuous. In this study, the results showed a lower F statistic at the highest canopy cover density than that obtained at the site with the highest canopy cover density in Rittger et al. (2020). This was probably due to the temporal distribution of the ASO validation dataset; flights are temporally focused after peak SWE occurs, when snow is more likely to be only on the ground and no longer on top of the canopy as is observed following storm events. SPIReS was also validated by Bair et al. (2021a) using an ASO dataset smaller than that used herein, and the results showed that the F statistic fell to approximately 80% for dense canopies; the dataset utilized in that study contained scenes representing only California.

The three Landsat approaches validated in this study all involve the use of different canopy correction methods. SPIReS and OLISCAG produced nearly identical RMSE variabilities associated with the canopy cover density, exhibiting relatively low RMSE values at low canopy cover densities and high RMSE values at the highest canopy cover densities compared to those obtained with the USGS Collection 1 fSCA product. SCAG had the most robust canopy cover correction for the Landsat products when ranked based on the minimum snow cover estimate bias and RMSE across all canopy cover densities. From the example shown in Fig. 6, SPIReS Landsat showed the lowest snow cover fraction bias under a forest canopy, though Fig. 4 indicates the near-equal performances of SPIReS Landsat and OLISCAG. The USGS product employs a spatial replacement step different from that of SPIReS Landsat (Sect. 4.1.5). This approach is the likely reason behind the higher F statistics observed for the USGS product at relatively high canopy cover densities before its snow detection ability dropped off, which is similar to the trends observed for the other products. Above a canopy cover fraction of approximately 0.65, none of the Landsat algorithms reliably mapped snow cover under the forest canopy, though few pixels were available for testing the algorithm performances under very dense canopy cover conditions. At canopy cover fractions ranging from 0.5 to 0.6, viewable snow cover mapping from multispectral optical satellite data becomes challenging if the mapping process is conducted based only on the spectral characteristics of

individual pixels. Ancillary spatial or other data are needed to improve snow cover estimates in pixels containing dense canopy cover. At these extremely high canopy cover densities, it is not only difficult to detect snow but also difficult to correct the actual fractional amount of snow present on the ground.

All approaches considered herein estimated more snow cover in pixels with dense canopy cover than the lidar validation dataset. It is unclear if these overestimates were caused by the canopy correction methods inherent to the remote sensing products, an issue associated with a lack of ground returns from the lidar in some dense forest canopy locations skewing the analysis, or both. At the meter scale, airborne lidar with typical point densities do not receive ground returns from all pixels covered by dense forest canopy (Zheng et al., 2016). ASO is also known to not always receive ground returns for all grid cells, and this issue is most prevalent for heavily forested locations. Cao et al. (2018) acknowledge that ASO ground point densities decrease non-linearly as canopy cover and vegetation height increase. Across all forested locations analyzed by Currier et al. (2019), 17% of the forested ASO pixels have no ground returns. It is likely that some of the positive biases reported herein for snow cover mapping under dense canopies by the remote sensing products are due to the FN ASO snow depth returns at the 3 m scale reducing the ASO fSCA values at the validation resolution.

The USGS Level-3 fSCA canopy correction method predated recent studies that have shown that forest snow cover is dependent on both the time of year and the type of forest. Forest dynamics are complex; different accumulation and melt patterns can be observed depending on specific forest characteristics (Dickerson-Lange et al., 2021), and variabilities arise in the relationship between forest fSCA values and adjacent open-area fSCA values due to various forest dynamics controlled by the canopy cover density, temperature, and aspect (Safa et al., 2021). Both of these past studies observed sparser late-season snow cover in denser canopy-covered areas. ASO usually performs springtime data acquisitions; at this time, the forest snow cover is more variable than that in mid-winter. Our study highlights and confirms that fSCA values below 1 are pervasive under forest canopies and that more complex canopy correction methods are needed if estimates of snow cover on the ground under forest canopies are to be improved. Additionally, snow present on the ground is simply not detectable under canopy cover fractions above 0.65, though snow in the canopy can often result in positive snow detections. Additional spatial data and ancillary snow information may help significantly improve our ability to map snow on the ground under dense forest canopies.

Regarding the MODIS and VIIRS products, due to their canopy correction methods and ability to integrate surface information from multi-day measurements obtained at various sensor zenith angles, the spectral-unmixing approaches showed improved snow detection abilities under high canopy

cover fractions compared to the standard products and the Landsat products. Additionally, the larger pixel sizes in the MODIS and VIIRS products allow canopy gap areas where snow detection for $fSCA > 0.1$ is trivial to be integrated in many pixels that contain canopy cover. In the Landsat products, varying bias patterns associated with the canopy cover density were observed under the same approaches; this finding may have been influenced by scale-dependent differences in the canopy cover distribution across the study area. There is a tradeoff between the aggressiveness (i.e., correcting to $fSCA = 1$) of the canopy correction method employed and the overall bias level observed in the results derived across the entire scene, potentially inducing major spatial issues when estimating snow cover fractions. Raleigh et al. (2013) and Rittger et al. (2020) previously reported a similar issue, which was particularly problematic when the canopy cover density exceeded the viewable snow cover fraction.

Full-waveform lidar data can be used to parameterize the viewable gap fraction in forests (Liu et al., 2008; Xin et al., 2012) to set an a priori expectation of the maximum viewable snow for a canopy correction step. While we used only a lidar snow depth product with a spatial resolution of 3 m, as no full-waveform dataset was available, good models exist for understanding what nadir and off-nadir sensors can see while considering a theoretical maximum. With original, full-waveform lidar data, one can also derive the necessary parameters for gap fraction modeling (Morsdorf et al., 2006; Zhao et al., 2012). SPIReS enables users to make parameterization adjustments for various canopy crown sizes and tree sizes in the fSCA canopy correction step, a procedure not possible with the SCAG or USGS products. Analyses with lidar datasets constructed in ranges like the Olympic Mountains could also shed more light on snow cover conditions in dense forests.

6.4 Snow-covered area insights

All of the spectral-unmixing approaches considered herein exhibited significant negative biases at high snow cover fractions. We posit that this finding can be attributed to two issues. First, it is impossible to obtain positive biases for fully snow-covered pixels, as snow cover cannot exceed $fSCA = 1$. Second, it is difficult to find a spectral-unmixing solution for $fSCA = 1$ that is substantially better than the solutions available for slightly lower snow cover fractions when dealing with many pixels. This is especially true when shading is present in the pixels, as shading has been shown to significantly lower the apparent albedo and snow cover reflectance (Bair et al., 2022).

The combination of systematic snow cover overestimates in forested areas with systematic underestimates of alpine snow cover led to the overall bias estimates being close to zero for all spectral-unmixing products. The spectral-mixture analysis methods, when applied to the Landsat and MODIS products, exhibited the best performances by achieving snow

cover products with low bias and with the best results across the assessed snow cover and canopy cover ranges. Error images, like those shown in Fig. 6, enabled us to identify systematic errors in snow cover fraction estimates and update the models, thus supporting a continuous-development approach to snow mapping. For example, we discovered that the opposing highly biased estimates derived in pixels with dense canopy cover and high fractional snow cover conditions can offset each other to generate an overall low bias. Figure 6 shows a spatial pattern in which underestimates (blue) are generally located in canopy-free areas and overestimates (red) are generally located in canopy-covered areas. The Landsat products consistently overestimated the snow cover fraction under dense canopy cover conditions and incorrectly detected snow around the snowpack boundaries near the lowest snow cover fractions. A possible explanation for this finding is that the interactions among the ground instantaneous field of view (GIFOV), point spread function, and pixel size led to pixel overlaps in these regions and to snow being identified within the GIFOV but outside the final pixel ground sample distance, thus causing FP detections and snow fraction overestimates; alternatively, the ASO snow detection map may be negatively biased.

6.5 View angle insights

A surprising result obtained from this study is the insensitivity of the snow mapping algorithms to the view angle of the MODIS or VIIRS sensor, given previous findings of MODSCAG view angle sensitivities with respect to forests (Rittger et al., 2020). However, Rittger et al. (2020) investigated raw or initial retrievals from MODSCAG, while both STC-MODSCAG and SPIReS MODIS incorporate pixel-based weighting schemes designed in consideration of the sensor view angle (Dozier et al., 2008). The VNP10 product showed some increasing RMSE values as the view angle increased, but this trend was not monotonic, and the lowest RMSE values were observed in the view angle range of $\sim 20\text{--}30^\circ$. However, both the corrected and the uncorrected VNP10 and MOD10 results exhibited relatively large biases at the largest view angles compared to the STC-MODSCAG and SPIReS results. We expected to see a stronger relationship between the view angle and errors in the standard products than in the products constructed using spectral-unmixing algorithms. A possible explanation is that the band ratio method experiences reduced view angle impacts because (1) both the VIS and the SWIR observations are affected and (2) dividing the VIS/SWIR reflectance difference by the sum of the VIS/SWIR reflectance (originally designed as a way to account for atmospheric differences when NDSI is applied to derived top-of-atmosphere reflectance) compensates for the view-angle-related errors.

Both STC-MODSCAG and SPIReS include temporal weighting and smoothing routines that weight data collected at nadir view angles higher than data collected at off-nadir

view angles. The fact that the view angle was not found to be strongly or consistently related to the error statistics indicates that these weighting schemes are effective. The coarsening of the MODIS and VIIRS products to the 2 km scale for use in our evaluations may have also minimized the view angle effect by increasing the pixel size.

6.6 Landsat vs. MODIS insights

In the study area, the Landsat-derived data contained significantly more canopy-free pixels than canopy-covered pixels compared to the coarser-resolution MODIS and VIIRS products (Fig. 4d). The 30 m scale observations lend credence to the value of techniques that can leverage canopy-free observations corresponding to locations at which MODIS cannot obtain canopy-free observations, thus improving our ability to detect various snow properties from space (Rittger et al., 2021b). However, as the canopy cover increases, all available algorithms face challenges when mapping snow; the detection abilities of these algorithms deteriorate rapidly with increasing canopy cover conditions. The *F*-statistic values decreased with increasing canopy cover densities for all Landsat products (Fig. 5g), implying that Landsat cannot identify all snow in forested landscapes and is thus an imperfect validation measure for coarser-resolution products. The ability of lidar instruments to both penetrate forest canopies and measure snow at sufficiently fine spatial scales to eliminate the need for fSCA and instead produce binary snow maps provides lidar-based methods with the improved ability to validate other snow products, such as those derived from multispectral sensors in forested areas. Prior studies have also shown that high-spatial-resolution commercial satellite data with spatial scales ranging from 0.5–4.0 m, the same spatial scales as those of lidar data, can be used to reliably map snow cover fractions for use in validations performed in canopy-free areas and to reliably detect snow cover presence under canopies; however, high-spatial-resolution commercial satellite data cannot be used to measure snow cover fractions under moderate canopy cover conditions (Bair et al., 2016, 2021a). Airborne lidar data and spaceborne high-resolution commercial data provide alternative validation solutions to using standard multispectral satellite data (e.g., Landsat and Sentinel-2 data).

7 Conclusion

The process by which snow cover is mapped using data collected by multispectral satellites has matured through the development of a variety of methods. Snow cover varies at a finer spatial resolution than that captured by multispectral sensors; thus, understanding how well various methods work across a range of snow cover fractions and in a variety of landscapes is critically important for recognizing global snow mapping capabilities. In this study, we examined how

well various products perform across various canopy cover densities, per-pixel fractional snow cover conditions, satellite view angles, and global snow type classifications. Supporting previous work, we found that spectral-unmixing algorithms perform better than standard NDSI-based products. Aerial lidar retrievals indicated that this finding holds true across a diverse range of snow and forest cover conditions and among all global seasonal snow cover classifications. Spectral-unmixing methods have reached a level of readiness that allows them to be deployed with modern computing techniques to advance snow cover mapping at the global scale.

Code and data availability. All Airborne lidar datasets were obtained from NSIDC (<https://nsidc.org/data/aso>; Painter et al., 2016) and ASO, Inc. (<https://data.airbornesnowobservatories.com/>; Painter et al., 2016). The key tables which match individual ASO lidar flights to the MODIS and VIIRS tiles, Landsat path/rows, and Landsat ARD tiles are available as a Supplement to this paper. The canopy cover data used in the validation are publicly available at <https://www.mrlc.gov/data> (Coulston et al., 2012). The sensor view angle data came from publicly available MOD09GA and VNP09GA datasets from NASA DAACs. The VNP10A1F (<https://doi.org/10.5067/VIIRS/VNP10A1F.001>; Riggs et al., 2019) and MOD10A1F (<https://doi.org/10.5067/MODIS/MOD10A1F.061>; Hall and Riggs, 2020) datasets were downloaded from NSIDC in May 2022. The SPIReS datasets used in this analysis are permanently stored with DOIs: MODIS WUS SPIReS DOI (<https://doi.org/10.21424/R4H05T>, Bair and Stilling, 2022) and Landsat 8 SPIReS DOI (<https://doi.org/10.21424/R4C62H>, Stilling and Bair, 2022). The SPIReS codebase is publicly available on GitHub with a tag for the version used in this validation analysis (<https://github.com/edwardbair/SPIRES/releases/tag/v1.1>, last access: 29 June 2022). The STC-MODSCAG and OLISCAG data from this paper are permanently stored on Zenodo with the following DOI (<https://doi.org/10.5281/zenodo.7510861>, Rittger, 2023). The SCAG code is currently closed-source; however, the MODSCAG data have been accepted by the NSIDC User Working Group and are supported by NSIDC user services (nsidc@nsidc.org).

Supplement. The supplement related to this article is available online at: <https://doi.org/10.5194/tc-17-567-2023-supplement>.

Author contributions. This paper was a team effort and is the result of the meaningful contributions of each author. The author contributions, according to CRediT taxonomy, are as follows: TS contributed to all 14 contributor roles. KR contributed to funding acquisition, formal analysis, software, methodology, validation, and writing (original, review, and editing). MSR contributed to software, validation, and writing (original, review, and editing). AM contributed to writing (original, review, and editing). RED contributed resources and funding acquisition. EHB contributed to all 14 contributor roles.

Competing interests. At least one of the (co-)authors is a member of the editorial board of *The Cryosphere*. The peer-review process was guided by an independent editor, and the authors also have no other competing interests to declare.

Disclaimer. Publisher's note: Copernicus Publications remains neutral with regard to jurisdictional claims in published maps and institutional affiliations.

Acknowledgements. This material is based upon work supported under the US Army Research, Development, Test and Evaluation Program, Program Element 0602144A, under the authority of the Broad Agency Announcement Program and the Cold Regions Research and Engineering Laboratory (ERDC CRREL), contract no. W913E521C0001. Timbo Stilling and Edward Bair were supported by NASA awards 80NSSC21K0997, 80NSSC20K1722, 80NSSC20K1349, 80NSSC18K1489, and 80NSSC21K0620. Mark S. Raleigh was supported in part by funding from NASA under grants 80NSSC22K0685 and 80NSSC22K0928. Karl Rittger was supported by funding from NASA under grants 80NSSC18K0427, 80NSSC22K0703, 80NSSC22K0929, 80NSSC20K1721, and supplements to support Snow Today at NSIDC as well as NOAA NA18OAR4590367. Mary Jo Brodzik processed the MODSCAG data used in this paper.

Financial support. This material is based upon work supported under the US Army Research, Development, Test and Evaluation Program (Program Element 0602144A), under the authority of the Broad Agency Announcement Program and the Cold Regions Research and Engineering Laboratory (ERDC CRREL) (contract no. W913E521C0001). Timbo Stilling and Edward Bair were supported by NASA (grant nos. 80NSSC21K0997, 80NSSC20K1722, 80NSSC20K1349, 80NSSC18K1489, and 80NSSC21K0620). Mark S. Raleigh was supported in part by funding from NASA (grant nos. 80NSSC22K0685 and 80NSSC22K0928). Karl Rittger was supported by funding from NASA (grant nos. 80NSSC18K0427, 80NSSC22K0703, 80NSSC22K0929, 80NSSC20K1721) and supplements to support Snow Today at NSIDC as well as NOAA (grant no. NA18OAR4590367).

Review statement. This paper was edited by Franziska Koch and reviewed by Roswitha Stolz and one anonymous referee.

References

- Aalstad, K., Westermann, S., and Bertino, L.: Evaluating satellite retrieved fractional snow-covered area at a high-Arctic site using terrestrial photography, *Remote Sens. Environ.*, 239, 111618, <https://doi.org/10.1016/j.rse.2019.111618>, 2020.
- Adams, J. B., Smith, M. O., and Johnson, P. E.: Spectral Mixture Modeling – a New Analysis of Rock and Soil Types at the Viking Lander-1 Site, *J. Geophys. Res.-Sol. Ea.*, 91, 8098–8112, <https://doi.org/10.1029/JB091iB08p08098>, 1986.

- Armstrong, R. L., Rittger, K., Brodzik, M. J., Racoviteanu, A., Barrett, A. P., Singh Khalsa, S.-J., Raup, B., Hill, A. F., Khan, A. L., Wilson, A. M., Kayastha, R. B., Fetterer, F., and Armstrong, B.: Runoff from glacier ice and seasonal snow in High Asia: separating melt water sources in river flow, *Reg. Environ. Change*, 19, 1249–1261, <https://doi.org/10.1007/s10113-018-1429-0>, 2018.
- Ault, T. W., Czajkowski, K. P., Benko, T., Coss, J., Struble, J., Sponberg, A., Templin, M., and Gross, C.: Validation of the MODIS snow product and cloud mask using student and NWS cooperative station observations in the Lower Great Lakes Region, *Remote Sens. Environ.*, 105, 341–353, <https://doi.org/10.1016/j.rse.2006.07.004>, 2006.
- Bair, E. and Stillinger, T.: SPIReS: Western USA snow cover and snow surface properties, water years 2001–2021, UCSB [data set], <https://doi.org/10.21424/R4H05T>, 2022.
- Bair, E. H., Rittger, K., Davis, R. E., Painter, T. H., and Dozier, J.: Validating reconstruction of snow water equivalent in California’s Sierra Nevada using measurements from the NASA Airborne Snow Observatory, *Water Resour. Res.*, 52, 8437–8460, <https://doi.org/10.1002/2016wr018704>, 2016.
- Bair, E. H., Rittger, K., Skiles, S. M., and Dozier, J.: An Examination of Snow Albedo Estimates From MODIS and Their Impact on Snow Water Equivalent Reconstruction, *Water Resour. Res.*, 55, 7826–7842, <https://doi.org/10.1029/2019wr024810>, 2019.
- Bair, E. H., Stillinger, T., and Dozier, J.: Snow Property Inversion From Remote Sensing (SPIReS): A Generalized Multi-spectral Unmixing Approach With Examples From MODIS and Landsat 8 OLI, *Ieee T. Geosci. Remote*, 59, 7270–7284, <https://doi.org/10.1109/TGRS.2020.3040328>, 2021a.
- Bair, E. H., Stillinger, T., Rittger, K., and Skiles, S. M.: COVID-19 Lockdowns Show Reduced Pollution on Snow and Ice in the Indus River Basin, *P. Natl. Acad. Sci. USA*, 118, e2101174118, <https://doi.org/10.1073/pnas.2101174118>, 2021b.
- Bair, E. H., Dozier, J., Stern, C., LeWinter, A., Rittger, K., Savagian, A., Stillinger, T., and Davis, R. E.: Divergence of apparent and intrinsic snow albedo over a season at a sub-alpine site with implications for remote sensing, *The Cryosphere*, 16, 1765–1778, <https://doi.org/10.5194/tc-16-1765-2022>, 2022.
- Baldrige, A. M., Hook, S. J., Grove, C. I., and Rivera, G.: The ASTER spectral library version 2.0, *Remote Sens. Environ.*, 113, 711–715, <https://doi.org/10.1016/j.rse.2008.11.007>, 2009.
- Bormann, K. J., Brown, R. D., Derksen, C., and Painter, T. H.: Estimating snow-cover trends from space, *Nat. Clim. Change*, 8, 923–927, <https://doi.org/10.1038/s41558-018-0318-3>, 2018.
- Branham, R. L. (Ed.): *Scientific Data Analysis: An Introduction to Overdetermined Systems*, Springer New York, New York City, NY, 1990.
- Campagnolo, M. L. and Montaña, E. L.: Estimation of Effective Resolution for Daily MODIS Gridded Surface Reflectance Products, *Ieee T. Geosci. Remote*, 52, 5622–5632, <https://doi.org/10.1109/TGRS.2013.2291496>, 2014.
- Cao, Q., Painter, T. H., Currier, W. R., Lundquist, J. D., and Lettenmaier, D. P.: Estimation of Precipitation over the OLYMPEX Domain during Winter 2015/16, *J. Hydrometeorol.*, 19, 143–160, <https://doi.org/10.1175/JHM-D-17-0076.1>, 2018.
- Clark, M. P., Hendriks, J., Slater, A. G., Kavetski, D., Anderson, B., Cullen, N. J., Kerr, T., Hreinsson, E. O., and Woods, R. A.: Representing spatial variability of snow water equivalent in hydrologic and land-surface models: A review, *Water Resour. Res.*, 47, W07539, <https://doi.org/10.1029/2011wr010745>, 2011.
- Coulston, J. W., Moisen, G. G., Wilson, B. T., Finco, M. V., Cohen, W. B., Brewer, C. K., Modeling percent tree canopy cover – A pilot study: *Photogramm. Eng. Remote Sens.*, 78, 715–727, <https://doi.org/10.14358/PERS.78.7.715>, 2012 (data available at: https://s3-us-west-2.amazonaws.com/mlrc/nlcd_2016_treecanopy_2019_08_31.zip, last access: 20 June 2021).
- Currier, W. R., Pflug, J., Mazzotti, G., Jonas, T., Deems, J. S., and Bormann, K. J.: Comparing aerial lidar observations with terrestrial lidar and snow-probe transects from NASA’s 2017 SnowEx campaign, *Water Resour. Res.*, 55, 6285–6294, <https://doi.org/10.1029/2018WR024533>, 2019.
- Deems, J. S., Painter, T. H., Barsugli, J. J., Belnap, J., and Udall, B.: Combined impacts of current and future dust deposition and regional warming on Colorado River Basin snow dynamics and hydrology, *Hydrol. Earth Syst. Sci.*, 17, 4401–4413, <https://doi.org/10.5194/hess-17-4401-2013>, 2013a.
- Deems, J. S., Painter, T. H., and Finnegan, D. C.: Lidar measurement of snow depth: a review, *J. Glaciol.*, 59, 467–479, <https://doi.org/10.3189/2013JG12J154>, 2013b.
- Dickerson-Lange, S. E., Vano, J. A., Gersonde, R., and Lundquist, J. D.: Ranking Forest Effects on Snow Storage: A Decision Tool for Forest Management, *Water Resour. Res.*, 57, e2020WR027926, <https://doi.org/10.1029/2020WR027926>, 2021.
- Dozier, J.: Spectral Signature of Alpine Snow Cover from the Landsat Thematic Mapper, *Remote Sens. Environ.*, 28, 9, [https://doi.org/10.1016/0034-4257\(89\)90101-6](https://doi.org/10.1016/0034-4257(89)90101-6), 1989.
- Dozier, J., Schneider, S. R., and McGinnis, D. F.: Effect of Grain-Size and Snowpack Water Equivalence on Visible and near-Infrared Satellite-Observations of Snow, *Water Resour. Res.*, 17, 1213–1221, <https://doi.org/10.1029/WR017i004p01213>, 1981.
- Dozier, J., Painter, T. H., Rittger, K., and Frew, J. E.: Time-space continuity of daily maps of fractional snow cover and albedo from MODIS, *Adv. Water Resour.*, 31, 1515–1526, <https://doi.org/10.1016/j.advwatres.2008.08.011>, 2008.
- Feng, S. and Hu, Q.: Changes in winter snowfall/precipitation ratio in the contiguous United States, *J. Geophys. Res.-Atmos.*, 112, D15109, <https://doi.org/10.1029/2007JD008397>, 2007.
- Guan, B., Molotch, N. P., Waliser, D. E., Jepsen, S. M., Painter, T. H., and Dozier, J.: Snow water equivalent in the Sierra Nevada: blending snow sensor observations with snowmelt model simulations, *Water Resour. Res.*, 49, 5029–5046, <https://doi.org/10.1002/wrcr.20387>, 2013.
- Hall, D. K. and Riggs, G. A.: Accuracy assessment of the MODIS snow products, *Hydrol. Process.*, 21, 1534–1547, <https://doi.org/10.1002/hyp.6715>, 2007.
- Hall, D. K. and Riggs, G. A.: MODIS/Terra CGF Snow Cover Daily L3 Global 500m SIN Grid, Version 61, Boulder, Colorado USA, NASA National Snow and Ice Data Center Distributed Active Archive Center [data set], <https://doi.org/10.5067/MODIS/MOD10A1F.061>, 2020.
- Hall, D. K., Riggs, G. A., Salomonson, V. V., DiGirolamo, N. E., and Bayr, K. J.: MODIS snow-cover products, *Remote Sens. Environ.*, 83, 181–194, [https://doi.org/10.1016/S0034-4257\(02\)00095-0](https://doi.org/10.1016/S0034-4257(02)00095-0), 2002.
- Hall, D. K., Riggs, G. A., Foster, J. L., and Kumar, S. V.: Development and evaluation of a cloud-gap-filled MODIS daily

- snow-cover product, *Remote Sens. Environ.*, 114, 496–503, <https://doi.org/10.1016/j.rse.2009.10.007>, 2010.
- Hall, D. K., Riggs, G. A., DiGirolamo, N. E., and Román, M. O.: Evaluation of MODIS and VIIRS cloud-gap-filled snow-cover products for production of an Earth science data record, *Hydrol. Earth Syst. Sci.*, 23, 5227–5241, <https://doi.org/10.5194/hess-23-5227-2019>, 2019.
- Hansen, J. and Nazarenko, L.: Soot climate forcing via snow and ice albedos, *P. Natl. Acad. Sci. USA.*, 101, 423–428, <https://doi.org/10.1073/pnas.2237157100>, 2004.
- Härer, S., Bernhardt, M., Siebers, M., and Schulz, K.: On the need for a time- and location-dependent estimation of the NDSI threshold value for reducing existing uncertainties in snow cover maps at different scales, *The Cryosphere*, 12, 1629–1642, <https://doi.org/10.5194/tc-12-1629-2018>, 2018.
- Homer, C., Huang, C. Q., Yang, L. M., Wylie, B., and Coan, M.: Development of a 2001 National Land-Cover Database for the United States, *Photogramm. Eng. Rem. S.*, 70, 829–840, <https://doi.org/10.14358/Pers.70.7.829>, 2004.
- Immerzeel, W. W., van Beek, L. P. H., and Bierkens, M. F. P.: Climate Change Will Affect the Asian Water Towers, *Science*, 328, 1382–1385, <https://doi.org/10.1126/science.1183188>, 2010.
- Immerzeel, W. W., Lutz, A. F., Andrade, M., Bahl, A., Biemans, H., Bolch, T., Hyde, S., Brumby, S., Davies, B. J., Elmore, A. C., Emmer, A., Feng, M., Fernandez, A., Haritashya, U., Kargel, J. S., Koppes, M., Kraaijenbrink, P. D. A., Kulkarni, A. V., Mayewski, P. A., Nepal, S., Pacheco, P., Painter, T. H., Pellicciotti, F., Rajaram, H., Rupper, S., Sinisalo, A., Shrestha, A. B., Viviroli, D., Wada, Y., Xiao, C., Yao, T., and Baillie, J. E. M.: Importance and vulnerability of the world's water towers, *Nature*, 577, 364, <https://doi.org/10.1038/s41586-019-1822-y>, 2020.
- Justice, C. O., Roman, M. O., Csaszar, I., Vermote, E. F., Wolfe, R. E., Hook, S. J., Friedl, M., Wang, Z. S., Schaaf, C. B., Miura, T., Tschudi, M., Riggs, G., Hall, D. K., Lyapustin, A. I., Devadiga, S., Davidson, C., and Masuoka, E. J.: Land and cryosphere products from Suomi NPP VIIRS: Overview and status, *J. Geophys. Res.-Atmos.*, 118, 9753–9765, <https://doi.org/10.1002/jgrd.50771>, 2013.
- Klein, A. G. and Barnett, A. C.: Validation of daily MODIS snow cover maps of the Upper Rio Grande River Basin for the 2000–2001 snow year, *Remote Sens. Environ.*, 86, 162–176, [https://doi.org/10.1016/S0034-4257\(03\)00097-X](https://doi.org/10.1016/S0034-4257(03)00097-X), 2003.
- Klein, A. G., Hall, D. K., and Riggs, G. A.: Improving snow cover mapping in forests through the use of a canopy reflectance model, *Hydrol. Process.*, 12, 1723–1744, [https://doi.org/10.1002/\(Sici\)1099-1085\(199808/09\)12:10/11<1723::Aid-Hyp691>3.0.Co;2-2](https://doi.org/10.1002/(Sici)1099-1085(199808/09)12:10/11<1723::Aid-Hyp691>3.0.Co;2-2), 1998.
- Lettenmaier, D. P., Alsdorf, D., Dozier, J., Huffman, G. J., Pan, M., and Wood, E. F.: Inroads of remote sensing into hydrologic science during the WRR era, *Water Resour. Res.*, 51, 7309–7342, <https://doi.org/10.1002/2015wr017616>, 2015.
- Liston, G. E.: Representing subgrid snow cover heterogeneities in regional and global models, *J. Climate*, 17, 1381–1397, [https://doi.org/10.1175/1520-0442\(2004\)017<1381:Rsschi>2.0.Co;2](https://doi.org/10.1175/1520-0442(2004)017<1381:Rsschi>2.0.Co;2), 2004.
- Liu, J., Woodcock, C. E., Melloh, R. A., Davis, R. E., McKenzie, C., and Painter, T. H.: Modeling the view angle dependence of gap fractions in forest canopies: Implications for mapping fractional snow cover using optical remote sensing, *J. Hydrometeorol.*, 9, 1005–1019, <https://doi.org/10.1175/2008JHM866.1>, 2008.
- Liu, J. C., Melloh, R. A., Woodcock, C. E., Davis, R. E., and Ochs, E. S.: The effect of viewing geometry and topography on viewable gap fractions through forest canopies, *Hydrol. Process.*, 18, 3595–3607, <https://doi.org/10.1002/hyp.5802>, 2004.
- Lundquist, J. D., Chickadel, C., Cristea, N., Currier, W. R., Henn, B., Keenan, E., and Dozier, J.: Separating snow and forest temperatures with thermal infrared remote sensing, *Remote Sens. Environ.*, 209, 764–779, <https://doi.org/10.1016/j.rse.2018.03.001>, 2018.
- Mankin, J. S., Viviroli, D., Singh, D., Hoekstra, A. Y., and Diffenbaugh, N. S.: The potential for snow to supply human water demand in the present and future, *Environ. Res. Lett.*, 10, 114016, <https://doi.org/10.1088/1748-9326/10/11/114016>, 2015.
- Masson, T., Dumont, M., Dalla Mura, M., Sirguey, P., Gascoin, S., Dedieu, J. P., and Chanussot, J.: An Assessment of Existing Methodologies to Retrieve Snow Cover Fraction from MODIS Data, *Remote Sens.-Basel*, 10, 619, <https://doi.org/10.3390/rs10040619>, 2018.
- Maurer, E. P., Rhoads, J. D., Dubayah, R. O., and Lettenmaier, D. P.: Evaluation of the snow-covered area data product from MODIS, *Hydrol. Process.*, 17, 59–71, <https://doi.org/10.1002/hyp.1193>, 2003.
- Meerdink, S. K., Hook, S. J., Roberts, D. A., and Abbott, E. A.: The ECOSTRESS spectral library version 1.0, *Remote Sens. Environ.*, 230, 111196, <https://doi.org/10.1016/j.rse.2019.05.015>, 2019.
- Micheletty, P., Perrot, D., Day, G., and Rittger, K.: Assimilation of Ground and Satellite Snow Observations in a Distributed Hydrologic Model for Water Supply Forecasting, *J. Am. Water Resour. A.*, 58, 1030–1048, <https://doi.org/10.1111/1752-1688.12975>, 2021.
- Micheletty, P. D., Kinoshita, A. M., and Hogue, T. S.: Application of MODIS snow cover products: wildfire impacts on snow and melt in the Sierra Nevada, *Hydrol. Earth Syst. Sci.*, 18, 4601–4615, <https://doi.org/10.5194/hess-18-4601-2014>, 2014.
- Minder, J. R., Letcher, T. W., and Skiles, S. M.: An evaluation of high-resolution regional climate model simulations of snow cover and albedo over the Rocky Mountains, with implications for the simulated snow-albedo feedback, *J. Geophys. Res.-Atmos.*, 121, 9069–9088, <https://doi.org/10.1002/2016jd024995>, 2016.
- Molotch, N. P., Painter, T. H., Bales, R. C., and Dozier, J.: Incorporating remotely-sensed snow albedo into a spatially-distributed snowmelt model, *Geophys. Res. Lett.*, 31, L03501, <https://doi.org/10.1029/2003gl019063>, 2004.
- Morsdorf, F., Kötz, B., Meier, E., Itten, K. I., and Allgöwer, B.: Estimation of LAI and fractional cover from small footprint airborne laser scanning data based on gap fraction, *Remote Sens. Environ.*, 104.1, 50–61, <https://doi.org/10.1016/j.rse.2006.04.019>, 2006.
- Nolin, A. W.: Recent advances in remote sensing of seasonal snow, *J. Glaciol.*, 56, 1141–1150, <https://doi.org/10.3189/002214311796406077>, 2010.
- Nolin, A. W. and Dozier, J.: Estimating Snow Grain-Size Using Aviris Data, *Remote Sens. Environ.*, 44, 231–238, [https://doi.org/10.1016/0034-4257\(93\)90018-S](https://doi.org/10.1016/0034-4257(93)90018-S), 1993.

- Nolin, A. W., Dozier, J., and Mertes, L. A. K.: Mapping Alpine Snow Using a Spectral Mixture Modeling Technique, *Ann. Glaciol.*, 17, 121–124, <https://doi.org/10.3189/S0260305500012702>, 1993.
- Nolin, A. W., Sproles, E. A., Rupp, D. E., Crumley, R. L., Webb, M. J., Palomaki, R. T., and Mar, E.: New snow metrics for a warming world, *Hydrol. Process.*, 35, e14262, <https://doi.org/10.1002/hyp.14262>, 2021.
- Oaida, C. M., Reager, J. T., Andreadis, K. M., David, C. H., Leveo, S. R., Painter, T. H., Bormann, K. J., Trangsrud, A. R., Giroto, M., and Famiglietti, J. S.: A High-Resolution Data Assimilation Framework for Snow Water Equivalent Estimation across the Western United States and Validation with the Airborne Snow Observatory, *J. Hydrometeorol.*, 20, 357–378, <https://doi.org/10.1175/JHM-D-18-0009.1>, 2019.
- Painter, T. H., Roberts, D. A., Green, R. O., and Dozier, J.: The effect of grain size on spectral mixture analysis of snow-covered area from AVIRIS data, *Remote Sens. Environ.*, 65, 320–332, [https://doi.org/10.1016/S0034-4257\(98\)00041-8](https://doi.org/10.1016/S0034-4257(98)00041-8), 1998.
- Painter, T. H., Dozier, J., Roberts, D. A., Davis, R. E., and Green, R. O.: Retrieval of subpixel snow-covered area and grain size from imaging spectrometer data, *Remote Sens. Environ.*, 85, 64–77, [https://doi.org/10.1016/S0034-4257\(02\)00187-6](https://doi.org/10.1016/S0034-4257(02)00187-6), 2003.
- Painter, T. H., Rittger, K., McKenzie, C., Slaughter, P., Davis, R. E., and Dozier, J.: Retrieval of subpixel snow covered area, grain size, and albedo from MODIS, *Remote Sens. Environ.*, 113, 868–879, <https://doi.org/10.1016/j.rse.2009.01.001>, 2009.
- Painter, T. H., Bryant, A. C., and Skiles, S. M.: Radiative forcing by light absorbing impurities in snow from MODIS surface reflectance data, *Geophys. Res. Lett.*, 39, L17502, <https://doi.org/10.1029/2012gl052457>, 2012.
- Painter, T. H., Berisford, D. F., Boardman, J. W., Bormann, K. J., Deems, J. S., Gehrke, F., Hedrick, A., Joyce, M., Laidlaw, R., Marks, D., Mattmann, C., McGurk, B., Ramirez, P., Richardson, M., Skiles, S. M., Seidel, F. C., and Winstral, A.: The Airborne Snow Observatory: Fusion of scanning lidar, imaging spectrometer, and physically-based modeling for mapping snow water equivalent and snow albedo, *Remote Sens. Environ.*, 184, 139–152, <https://doi.org/10.1016/j.rse.2016.06.018>, 2016 (data available at: <https://nsidc.org/data/aso>, last access: 26 March 2021; <https://data.airbornesnowobservatories.com/>, last access: 12 February 2012).
- Raleigh, M. S., Rittger, K., Moore, C. E., Henn, B., Lutz, J. A., and Lundquist, J. D.: Ground-based testing of MODIS fractional snow cover in subalpine meadows and forests of the Sierra Nevada, *Remote Sens. Environ.*, 128, 44–57, <https://doi.org/10.1016/j.rse.2012.09.016>, 2013.
- Riggs, G., Hall, D. K., and Román, M. O.: VIIRS/NPP CGF Snow Cover Daily L3 Global 375m SIN Grid, Version 1, Boulder, Colorado USA, NASA National Snow and Ice Data Center Distributed Active Archive Center [data Set], <https://doi.org/10.5067/VIIRS/VNP10A1F.001>, 2019.
- Rittger, K.: Snow cover from spectral mixture analysis algorithm SCAG: OLI and MODIS (v2023.beta), Zenodo [data set], <https://doi.org/10.5281/zenodo.7510861>, 2023.
- Rittger, K. and Raleigh, M. S.: Snow Today, <https://nsidc.org/snow-today> (last access: 29 June 2022), 24 February 2020.
- Rittger, K., Painter, T. H., and Dozier, J.: Assessment of methods for mapping snow cover from MODIS, *Adv. Water Resour.*, 51, 367–380, <https://doi.org/10.1016/j.advwatres.2012.03.002>, 2013.
- Rittger, K., Bair, E. H., Kahl, A., and Dozier, J.: Spatial estimates of snow water equivalent from reconstruction, *Adv. Water Resour.*, 94, 345–363, <https://doi.org/10.1016/j.advwatres.2016.05.015>, 2016.
- Rittger, K., Raleigh, M. S., Dozier, J., Hill, A. F., Lutz, J. A., and Painter, T. H.: Canopy Adjustment and Improved Cloud Detection for Remotely Sensed Snow Cover Mapping, *Water Resour. Res.*, 56, e2019WR024914, <https://doi.org/10.1029/2019WR024914>, 2020.
- Rittger, K., Bormann, K. J., Bair, E. H., Dozier, J., and Painter, T. H.: Evaluation of VIIRS and MODIS Snow Cover Fraction in High-Mountain Asia Using Landsat 8 OLI, *Front. Remote Sens.*, 2, <https://doi.org/10.3389/frsen.2021.647154>, 2021a.
- Rittger, K., Krock, M., Kleiber, W., Bair, E. H., Brodzik, M. J., Stephenson, T. R., Rajagopalan, B., Bormann, K. J., and Painter, T. H.: Multi-sensor fusion using random forests for daily fractional snow cover at 30 m, *Remote Sens. Environ.*, 264, 112608, <https://doi.org/10.1016/j.rse.2021.112608>, 2021b.
- Roberts, D. A., Gardner, M., Church, R., Ustin, S., Scheer, G., and Green, R. O.: Mapping chaparral in the Santa Monica Mountains using multiple endmember spectral mixture models, *Remote Sens. Environ.*, 65, 267–279, [https://doi.org/10.1016/S0034-4257\(98\)00037-6](https://doi.org/10.1016/S0034-4257(98)00037-6), 1998.
- Romanov, P., Tarpley, D., Gutman, G., and Carroll, T.: Mapping and monitoring of the snow cover fraction over North America, *J. Geophys. Res.*, 108, 8619, <https://doi.org/10.1029/2002JD003142>, 2003.
- Rosenthal, W. and Dozier, J.: Automated Mapping of Montane Snow Cover at Subpixel Resolution From the Landsat Thematic Mapper, *Water Resour. Res.*, 115–130, <https://doi.org/10.1029/95WR02718>, 1996.
- Safa, H., Krogh, S. A., Greenberg, J., Kostadinov, T. S., and Harpold, A. A.: Unraveling the Controls on Snow Disappearance in Montane Conifer Forests Using Multi-Site Lidar, *Water Resour. Res.*, 57, e2020WR027522, <https://doi.org/10.1029/2020WR027522>, 2021.
- Salomonson, V. V. and Appel, I.: Estimating fractional snow cover from MODIS using the normalized difference snow index, *Remote Sens. Environ.*, 89, 351–360, <https://doi.org/10.1016/j.rse.2003.10.016>, 2004.
- Salomonson, V. V. and Appel, I.: Development of the Aqua MODIS NDSI fractional snow cover algorithm and validation results, *Ieee T. Geosci. Remote*, 44, 1747–1756, <https://doi.org/10.1109/Tgrs.2006.876029>, 2006.
- Selkowitz, D. J., Forster, R. R., and Caldwell, M. K.: Prevalence of Pure Versus Mixed Snow Cover Pixels across Spatial Resolutions in Alpine Environments, *Remote Sens.-Basel*, 6, 12478–12508, <https://doi.org/10.3390/rs61212478>, 2014.
- Selkowitz, D. J., Painter, T. H., Rittger, K. E., Schmidt, G., and Forster, R.: The USGS Landsat Snow Covered Area Products: Methods and Preliminary Validation, in: Automated Approaches for Snow and Ice Cover Monitoring Using Optical Remote Sensing, edited by: Selkowitz, D. J., The University of Utah, Salt Lake City, Utah, 76–119, 2017.
- Serquet, G., Marty, C., Dulex, J.-P., and Rebetez, M.: Seasonal trends and temperature dependence of the snowfall/precipitation-

- day ratio in Switzerland, *Geophys Res Lett*, 38, L07703, <https://doi.org/10.1029/2011GL046976>, 2011.
- Simard, M., Pinto, N., Fisher, J. B., and Baccini, A.: Mapping forest canopy height globally with spaceborne lidar, *J. Biophys. Res.*, 116, G04021, <https://doi.org/10.1029/2011JG001708>, 2011.
- Simic, A., Fernandes, R., Brown, R., Romanov, P., Park, W., Hall, D. K., and Ca, A. S. N. G.: Validation of MODIS, VEGETATION, and GOES plus SSM/I snow cover products over Canada based on surface snow depth observations, *Hydrol. Process.*, 836–838, <https://doi.org/10.1002/hyp.5509>, 2004.
- Sirguey, P., Mathieu, R., and Arnaud, Y.: Subpixel monitoring of the seasonal snow cover with MODIS at 250 m spatial resolution in the southern alps of New Zealand: Methodology and accuracy assessment, *Remote Sens. Environ.*, 113, 160–181, <https://doi.org/10.1016/j.rse.2008.09.008>, 2009.
- Skiles, S. M., Painter, T. H., Deems, J. S., Bryant, A. C., and Landry, C. C.: Dust radiative forcing in snow of the Upper Colorado River Basin: 2. Interannual variability in radiative forcing and snowmelt rates, *Water Resour. Res.*, 48, W07522, <https://doi.org/10.1029/2012wr011986>, 2012.
- Stewart, I. T., Cayan, D. R., and Dettinger, M. D.: Changes toward earlier streamflow timing across western North America, *J. Climate*, 18, 1136–1155, <https://doi.org/10.1175/Jcli3321.1>, 2005.
- Stilling, T. and Bair, E.: SPIReS: Landsat 8 snow cover and snow surface properties co-incident with 3 m LiDAR from the Airborne Snow Observatory, UCSB [data set], <https://doi.org/10.21424/R4C62H>, 2022.
- Stilling, T., Roberts, D. A., Collar, N. M., and Dozier, J.: Cloud Masking for Landsat 8 and MODIS Terra Over Snow-Covered Terrain: Error Analysis and Spectral Similarity Between Snow and Cloud, *Water Resour. Res.*, 55, 6169–6184, <https://doi.org/10.1029/2019wr024932>, 2019.
- Sturm, M. and Liston, G. E.: Revisiting the Global Seasonal Snow Classification: An Updated Dataset for Earth System Applications, *J. Hydrometeorol.*, 22, 2917–2938, <https://doi.org/10.1175/Jhm-D-21-0070.1>, 2021.
- Tong, R., Parajka, J., Komma, J., and Blöschl, G.: Mapping snow cover from daily Collection 6 MODIS products over Austria, *J. Hydrol.*, 590, 125548, <https://doi.org/10.1016/j.jhydrol.2020.125548>, 2020.
- Vikhamar, D. and Solberg, R.: Snow-cover mapping in forests by constrained linear spectral unmixing of MODIS data, *Remote Sens. Environ.*, 88, 309–323, <https://doi.org/10.1016/j.rse.2003.06.004>, 2003.
- Warren, S. G.: Optical-Properties of Snow, *Rev. Geophys.*, 20, 67–89, <https://doi.org/10.1029/RG020i001p00067>, 1982.
- Wickham, J., Stehman, S. V., Sorenson, D. G., Gass, L., and Dewitz, J. A.: Thematic accuracy assessment of the NLCD 2016 land cover for the conterminous United States, *Remote Sens. Environ.*, 257, 112357, <https://doi.org/10.1016/j.rse.2021.112357>, 2021.
- Xin, Q., Woodcock, C. E., Liu, J., Tan, B., Melloh, R. A., and Davis, R. E.: View angle effects on MODIS snow mapping in forests, *Remote Sens. Environ.*, 118, 50–59, <https://doi.org/10.1016/j.rse.2011.10.029>, 2012.
- Zemp, M., Frey, H., Gartner-Roer, I., Nussbaumer, S. U., Hoelzle, M., Paul, F., Haeblerli, W., Denzinger, F., Ahlstrom, A. P., Anderson, B., Bajracharya, S., Baroni, C., Braun, L. N., Caceres, B. E., Casassa, G., Cobos, G., Davila, L. R., Granados, H. D., Demuth, M. N., Espizua, L., Fischer, A., Fujita, K., Gadek, B., Ghazanfar, A., Hagen, J. O., Holmlund, P., Karimi, N., Li, Z. Q., Pelto, M., Pitte, P., Popovnin, V. V., Portocarrero, C. A., Prinz, R., Sangevar, C. V., Severskiy, I., Sigurosson, O., Soruco, A., Usabaliev, R., Vincent, C., and Correspondents, W. N.: Historically unprecedented global glacier decline in the early 21st century, *J. Glaciol.*, 61, 745, <https://doi.org/10.3189/2015JoG15J017>, 2015.
- Zhao, F., Strahler, A. H., Schaaf, C. L., Yao, T., Yang, X., Wang, Z., and Schull, M. A.: Measuring gap fraction, element clumping index and LAI in Sierra Forest stands using a full-waveform ground-based lidar, *Remote Sens. Environ.*, 125, 73–79, <https://doi.org/10.1016/j.rse.2012.07.007>, 2012.
- Zheng, Z., Kirchner, P. B., and Bales, R. C.: Topographic and vegetation effects on snow accumulation in the southern Sierra Nevada: a statistical summary from lidar data, *The Cryosphere*, 10, 257–269, <https://doi.org/10.5194/tc-10-257-2016>, 2016.